

Safety Considerations and Clinical Benefit Analysis for the Use of Elevated Acoustic
Output in Diagnostic Ultrasound Imaging

by

Bofeng Zhang

Department of Biomedical Engineering
Duke University

Date: _____

Approved:

Kathryn Nightingale, Supervisor

Gregg Trahey

Gianmarco Pinton

Junjie Yao

Nick Bottenus

Dissertation submitted in partial fulfillment of
the requirements for the degree of Doctor
of Philosophy in the Department of
Biomedical Engineering in the Graduate School
of Duke University

2021

ABSTRACT

Safety Considerations and Clinical Benefit Analysis for the Use of Elevated Acoustic Output in Diagnostic Ultrasound Imaging

by

Bofeng Zhang

Department of Biomedical Engineering
Duke University

Date: _____

Approved:

Kathryn Nightingale, Supervisor

Gregg Trahey

Gianmarco Pinton

Junjie Yao

Nick Bottenus

An abstract of a dissertation submitted in partial fulfillment of the requirements for the degree of Doctor of Philosophy in the Department of Biomedical Engineering in the Graduate School of Duke University

2021

Copyright by
Bofeng Zhang
2021

Abstract

Diagnostic ultrasound imaging has the advantages of being low cost, lacking ionizing radiation, and displaying output in real-time. It is often the imaging technique of choice when specifically interested in the liver, but it can suffer from poor image quality that results in images of reduced or no diagnostic value. Since failed ultrasound scans are often correlated with patient obesity and obesity is trending upwards in the US, this is a growing issue.

A fundamental cause for failed ultrasound scans is poor signal-to-noise ratio. To combat this, increasing diagnostic ultrasound strength or acoustic output is proposed. Previous work has demonstrated remarkable improvements specifically during ultrasonic harmonic shear wave elasticity imaging (SWEI) when using elevated Mechanical Index (MI), or energy, to quantify tissue stiffness. It is unclear, however, which one of the two ultrasonic pulses is impacted more by the body wall and benefits more from elevated MI given that SWEI sequences consist of a long push pulse and a short tracking pulse. In Chapter 3, an opposing window experiment was built and used to isolate the impacts of the body wall on the push and track beams. Track beams were found to be more affected by the presence of body walls and to benefit more from higher MI transmits.

In Chapter 4, 3D nonlinear ultrasound simulations and experimental measurements were used to estimate the range of *in situ* pressures that can occur during transcutaneous abdominal imaging, and to identify the sources of error when estimating *in situ* peak rarefaction pressures (PRP) using linear derating as specified by the MI guideline. Using simulations, it was found that for a large transmit aperture (F/1.5) MI consistently overestimated *in situ* PRP by 20-48%, due primarily to phase aberration. For a medium transmit aperture (F/3), the MI accurately estimated the *in situ* PRP to within 8%. For a small transmit aperture (F/5), MI consistently underestimated the *in situ* PRP by 32-50%, with peak locations occurring 1-2 cm before the focal depth, often within the body wall itself. The large variability across body wall samples and focal configurations demonstrates the limitations of the simplified linear derating scheme. The results suggest that patient specific *in situ* PRP estimation would allow for increases in transmit pressures, particularly for tightly focused beams, to improve diagnostic image quality while ensuring patient safety.

Tissue harmonic signal quality has been shown to improve with elevated acoustic pressure. The peak rarefaction pressure (PRP) for a given transmit, however, is limited by the FDA guideline for the mechanical index (MI). In Chapter 4, We demonstrated that the MI overestimates *in situ* PRP for tightly focused beams *in vivo* due primarily to phase aberration. In Chapter 5, we evaluate two spatial coherence-based image quality metrics, short-lag spatial coherence (SLSC) and harmonic short-lag spatial

coherence (HSC), as proxy estimates for phase aberration and assess their correlation with *in situ* PRP in simulations and experimentally when imaging through abdominal body walls. We demonstrate strong correlation between both spatial coherence-based metrics with *in situ* PRP ($r^2 = 0.77$ for HSC, $r^2 = 0.67$ for SLSC), an observation that could be leveraged in the future for patient-specific selection of acoustic output.

Dedication

To mom and dad for promoting curiosity and nurturing my desire to learn.

Contents

Abstract	iv
List of Tables	xii
List of Figures	xiii
Acknowledgements	xvi
1 Introduction.....	1
1.1 Motivation	2
1.2 Thesis Outline	5
2 Background	7
2.1 Acoustic Radiation Force (ARF) Based Elasticity Imaging.....	7
2.1.1 ARF Pushing Pulses	8
2.1.2 Tracking Pulse Approaches	9
2.2 Mechanical Index (MI).....	12
2.3 Tissue Harmonic Imaging (THI)	13
2.4 Spatial Coherence	15
2.5 Acoustic Clutter	16
3 Quantifying the Impact of Imaging through Body Walls on Shear Wave Elasticity Measurements	18
3.1 Introduction.....	18
3.2 Methods	21
3.2.1 Transducer and System Configuration	22
3.2.2 SWEI Data Acquisition	24

3.2.2.1 DAX Push and Track (Table 3.1: Imaging Combination 1).....	25
3.2.2.2 DAX Push with L7-4 Track (Table 3.1: Imaging Combination 2).....	26
3.2.2.3 L7-4 Push with DAX Track (Table 3.1: Imaging Combination 3).....	26
3.2.3 Spatial Coherence Data Acquisition	27
3.2.4 SWS Estimation.....	28
3.2.5 Peak Displacement and Jitter Estimation.....	29
3.2.6 MI Measurement	29
3.3 Results	30
3.4 Discussion.....	42
3.5 Conclusions	44
3.6 Conflict of Interest.....	45
3.7 Acknowledgements.....	45
4 Quantifying the Impact of Abdominal Body Wall on <i>in situ</i> Peak Rarefaction Pressure during Diagnostic Ultrasound Imaging.....	46
4.1 Introduction.....	46
4.2 Methods	48
4.2.1 Simulations.....	48
4.2.2 <i>In situ</i> Experiments.....	51
4.3 Results	53
4.3.1 Simulation Validation.....	53
4.3.1.1 Material Nonlinearity Parameter.....	54
4.3.1.2 Material Attenuation	55

4.3.1.3 Medium Aperture (F/3) Path Heterogeneity	56
4.3.1.4 Large Aperture (F/1.5) Path Heterogeneity	57
4.3.1.5 Small Aperture (F/5) Path Heterogeneity	59
4.3.2 Experimental Results	61
4.4 Discussion.....	64
4.5 Conclusions	69
4.6 Acknowledgements.....	70
5 On the Relationship between Spatial Coherence and <i>in situ</i> Pressure for Abdominal Imaging.....	71
5.1 Introduction.....	71
5.2 Methods	74
5.2.1 Simulations.....	74
5.2.2 <i>In situ</i> Experiments.....	78
5.2.3 Estimating Attenuation	81
5.2.3 Multiple Linear Regression.....	82
5.3 Results	82
5.3.1 Simulation Results.....	82
5.3.1.1 Fundamental Spatial Coherence	83
5.3.1.2 1-way Body Wall Simulations	84
5.3.1.3 Harmonic Spatial Coherence.....	85
5.3.2 Experimental Results	86
5.4 Discussion.....	91

5.5 Conclusions	96
5.6 Acknowledgements.....	97
6 Conclusions and Future Work.....	98
References	103
Biography.....	114

List of Tables

Table 3.1: 3 combinations of transducers used for push and track.....	22
Table 3.2: Push pulse parameters for the DAX and L7-4.....	24
Table 3.3: SWEI tracking parameters for the DAX and L7-4 transducers.....	25
Table 4.1: Simulated Tissue Acoustic Properties.....	51
Table 5.1: Simulated and Experimental Transducer Transmit Configuration.	74
Table 5.2: Simulated Tissue Acoustic Properties.....	75
Table 5.3: Regression Coefficient Between PRP/MIE and the Various Simulated Received Signals.....	89
Table 5.4: Multiple Linear Least Squares Model Fit.....	91

List of Figures

Figure 2.1: A simulated displacement field.....	8
Figure 2.2: Three types of shear wave tracking configurations.....	10
Figure 2.3: Reflected ultrasonic pulse signal from a point.....	15
Figure 3.1: Opposing window experimental setup.....	22
Figure 3.2: Control diagram for one-way synchronization from Sequoia system to Vantage system.	24
Figure 3.3: Percentage yield of successful SWS measurements as a function of ARFI push beam MI.....	30
Figure 3.4: Sample shear wave trajectories from acquisitions from varying push MI.....	31
Figure 3.5: SweiNet SWS uncertainty as function of push MI.....	32
Figure 3.6: Percentage yield of successful SWS measurements as the DAX harmonic SWE track pulse MI.....	33
Figure 3.7: Sample shear wave trajectories from acquisitions varying DAX track MI in one body wall.	34
Figure 3.8: SweiNet SWS uncertainty as function of track MI.....	35
Figure 3.9: Distributions of peak ARFI displacement amplitudes tracked.....	36
Figure 3.10: Mean and standard deviation of jitter	37
Figure 3.11: Mean track jitter magnitude.....	38
Figure 3.12: Theoretical Cramer-Rao Lower Bound	39
Figure 3.13: Harmonic spatial coherence.....	40
Figure 4.1: Sample image slice of abdominal wall	51
Figure 4.2: Experimental setup for scanning <i>in situ</i> PRP field.....	53

Figure 4.3: Experimentally measured MIE pressure waveforms from propagation through milk mixture	54
Figure 4.4: Simulated PRP magnitude and MIE.....	55
Figure 4.5: Simulated PRP magnitude and MIE.....	55
Figure 4.6: Simulated lateral-axial <i>in situ</i> PRP/MIE beam plot along the center elevation slice for an F/3 transmit	56
Figure 4.7: Simulated <i>in situ</i> PRP/MIE spatial distributions of an F/1.5 transmit.....	57
Figure 4.8: Simulated <i>in situ</i> PRP/MIE spatial distributions of an F/5 transmit.....	59
Figure 4.9: Peak intensity pressure waveform.....	62
Figure 4.10: Lateral-elevation transmit intensity beamwidth at PRP depth.....	63
Figure 4.11: <i>In situ</i> PRP/MIE measured through 9 body walls compared to that estimated by the MI	64
Figure 5.1: Experimental setup used to measure <i>in situ</i> PRP through a body wall sample.	78
Figure 5.2: Experimental setup used to acquire channel data for spatial coherence.....	80
Figure 5.3: Example clinical b-mode image of a pork belly sample used to segment the various tissue	81
Figure 5.4: Matching simulated <i>in situ</i> PRP/MIE waveforms, fundamental spatial coherence, and harmonic spatial coherence.....	82
Figure 5.5: <i>In situ</i> PRP/MIE plotted against various spatial coherence metrics.	83
Figure 5.6: Example experimentally measured spatial coherence curves at the axial focus	86
Figure 5.7: Coronal plane (elevation x lateral) map of the experimentally measured PRP magnitude at the axial depth of maximum PRP	87
Figure 5.8: The experimentally measured <i>in situ</i> PRP/MIE plotted against the SLSC	88

Figure 5.9: The r^2 value resulting from the linear regression line of best fit between experimentally measured spatial coherence and *in situ* PRP/MIE..... 89

Figure 5.10: Pork belly thickness plotted with the corresponding MIE. 90

Acknowledgements

I would like to thank Kathy for not giving up on me in addition to the guidance and support that she has given me throughout my time at Duke. Additionally, Kathy's enthusiasm for science and new knowledge has kept the flame of my academic curiosity bright.

I would also like to thank the other members of my committee, Gregg, Gianmarco, Nick, and Junjie, for their valuable input and guidance throughout this dissertation.

I would like to thank Mark and Ned Rouze for their valuable insight and suggestions during lab meetings.

The technical support from Mark and Ned Danieleley has also been critical for this dissertation. Thank you for helping me with computer issues even at the most inconvenient of times.

I would also like to thank the rest of Duke Ultrasound for putting up with my stupid questions, shenanigans, and making my time in graduate school the most memorable 6 years.

I would like to thank Siemens Healthineers for their in-kind technical support.

I would like to acknowledge the funding source NIH Grant R01 EB022106 for supporting my research and graduate studies.

1 Introduction

Ultrasound was first used in the imaging field to perform quality control testing on the internals of metal castings by Floyd Firestone in 1946 [1]. In 1949, George Ludwig applied the same one-dimensional ultrasound A-line technique in the human body for medical purposes to locate gallstones [2]. Then, in the 1950s, John Wild and John Reid published the first anatomical two-dimensional Brightness-mode (B-mode) ultrasound images used to characterize and diagnose breast tumors [3, 4]. B-mode medical diagnostic ultrasound systems were then commercialized in 1962 by Joseph Holmes, William Wright, and Ralph Meyerdirk [5]. More recently, in the late 1990s, acoustic radiation force (ARF) based techniques, such as acoustic radiation force impulse imaging (ARFI) and shear wave elasticity imaging (SWEI), which portray tissue mechanical properties instead of acoustic properties, were introduced to diagnostic medical ultrasound [6, 7]. Around this same time tissue harmonic imaging (THI), which detects second harmonic ultrasound signal generated inside the human subject during propagation, was developed [8] and applied to patients in the early 2000s [9]. Since its inception as a diagnostic tool, ultrasound imaging has seen continued development and remains a popular imaging modality due to its low cost, lack of ionizing radiation, and ability to be used in real-time. Today, ultrasound is often the first-line imaging technique

for abdominal regions and the imaging technique of choice when specifically interested in the liver [10, 11].

1.1 Motivation

Even though diagnostic ultrasound imaging has the advantages of being low cost, lacking ionizing radiation, displaying output in real-time and is the current standard-of-care when screening the liver for hepatocellular carcinoma (HCC) [12, 13], it can suffer from poor image quality. This drawback accounts for HCC screening being unable to diagnose 25-60% of patients [14-17]. Failed ultrasound HCC screens show correlation with patient obesity [18, 19]. Since more than 30% of the US adult population over the age of 20 are obese and trending upwards, this is a major and growing issue [20].

THI, the current clinical standard for hepatic ultrasound imaging [21], improves image quality compared to traditional fundamental mode through the reduction of clutter [8, 22-24]; however, THI can be hindered by poor signal-to-noise because harmonic signal is generated from nonlinear propagation at levels often 15-20 dB lower than the fundamental [9]. The harmonic signal is further lowered by the increased propagation depth needed to image larger patients. The logical solution for poor signal-to-noise ratio (SNR) arising from additive noise, such as electronic noise, is to increase signal strength. This is achieved by increasing the transmitted acoustic pressure, a

parameter which is typically quantified by the peak rarefactional pressure (PRP). The FDA guideline limiting *in situ* PRP is the Mechanical Index (MI) [25, 26] where $MI = PRP_{0.3}/\sqrt{f_{awf}}$. In the equation, $PRP_{0.3}$ is the PRP measured in deionized water and derated by 0.3 db/cm/MHz. f_{awf} is the acoustic working frequency, or the center frequency of the measured pulse. The FDA guidelines recommend maintaining $MI < 1.9$ [25], which results in this *de facto* upper limit for MI.

The work in this thesis investigates acoustic output specifically relating to hepatic diagnostic ultrasound imaging. First, the impact of performing hepatic SWEI imaging using elevated acoustic pressures is investigated. Next, the range of pressures that can occur *in vivo* for a given transmit configuration is quantified when imaging through different body walls. Lastly, an approach to estimate *in situ* PRPs that could be employed for real-time adaptive acoustic output optimization is developed.

In the context of ultrasonic hepatic SWEI imaging, measurement success has been shown to increase when using elevated PRP [27, 28]. In one study, liver shear wave speed (SWS) measurement success demonstrated increases of 27% across 25 human subjects when using tracking transmit configurations with an MI of 2.4 compared to the same configuration using an MI of 1.4 [27]. This study highlighted the potential clinical benefits of increasing MI for ultrasonic tracking beams during SWEI measurements. The scope of the study, however, only examined the effects of a specific tracking beam

configuration and was limited to two MI values. Because SWEI sequences consist of two distinct operations (pushing and tracking), acquisition failures could have been attributed to (1) insufficient ARF generation resulting in inadequate shear wave amplitude, and/or (2) distorted ultrasonic tissue motion tracking. Herein, an opposing window experimental setup that isolated body wall effects separately between the push and track SWEI operations was developed. Additionally, instead of using the tracking configuration of the previous study (STL-SWEI [29, 30]), a more commonly employed commercial track configuration was used (MTL-SWEI [31, 32]). The effects of imaging through body walls on the pushing and tracking operations of SWEI as a function of MI, spanning 5 different push beam MIs and 10 track beam MIs are independently assessed in Chapter 3.

Currently, the FDA guidelines effectively limit *in situ* PRP with the Mechanical Index (MI) to be less than 1.9 [25]. The MI is derived from a first order approximation of *in situ* PRP by linearly derating measurements made in water [33]. However, because tissue heterogeneities in sound speed, attenuation, density, and nonlinearity are present *in vivo*, the MI calculation can overestimate or/underestimate actual *in situ* acoustic output depending upon the body habitus and acoustic imaging window for any given patient. In the case of overestimation, the transmit pressure could be increased while remaining within the spirit of the FDA guidance, and the opposite is true in the case of

underestimation. In Chapter 4, 3D nonlinear ultrasound simulations and experimental measurements were performed to quantify the range of *in situ* pressures that can occur during transcutaneous abdominal imaging for specific transmit configurations, and to identify the sources of error when estimating the *in situ* PRP using linear derating as specified by the MI guideline.

Lastly, there are no methods for estimating *in situ* PRP in real-time that account for tissue heterogeneity. However, such a method would facilitate real-time, patient- and imaging-window specific adaptive transmit imaging to maximize SNR while staying within FDA guidelines for acoustic output. Chapter 5 investigates the correlation between a surrogate metric for phase aberration (spatial coherence) and decreases in *in situ* PRP arising from tissue heterogeneity. This work lays the foundation for higher transmit acoustic pressures to be safely utilized while following the spirit of the FDA guideline for MI.

1.2 Thesis Outline

Chapter 2 provides background information relevant to this work. Reviews of SWEI imaging and THI imaging, the development of the Mechanical Index (MI), and the theory of spatial coherence are provided.

Chapter 3 quantifies the effects of SWEI imaging through the body wall separately for the push and track beams using a clinical MTL-SWEI sequence in experimental phantom studies.

Chapter 4 uses 2D and 3D simulations to quantify the effects of the body wall on *in situ* PRP. The simulation findings are then validated with *ex vivo* phantom experimental measurements.

Chapter 5 takes the insight learned from the simulations in Chapter 4 to develop a coherence-based metric that is sensitive to body wall effects for use as a proxy to estimate *in situ* PRP in real-time. The correlation between the metric and *in situ* PRP is investigated with 2D simulations and validated with *ex vivo* phantom measurements.

Finally, **Chapter 6** summarizes the work presented in this thesis and outlines future directions.

2 Background

2.1 Acoustic Radiation Force (ARF) Based Elasticity Imaging

Acoustic radiation force (ARF) based elasticity imaging techniques, such as acoustic radiation force impulse (ARFI) imaging and shear wave elasticity imaging (SWEI) have been around since the late 1990s [6, 7, 35]. Unlike conventional B-mode imaging which utilizes the acoustic impedance differences between tissues as the mechanism for contrast, ARF based elasticity imaging techniques deploy two types of pulses in succession from a single transducer to generate images that portray tissue stiffness. The two types of pulses are a pushing pulse and tracking pulses. The pushing pulses are long duration focused ultrasonic pulses while the tracking pulses are shorter duration pulses similar to those used for B-mode imaging. A typical soft tissue response to an ARF excitation is portrayed in Figure 2.1. For ARFI imaging (blue in Figure 2.1d), relative differences in on-axis tissue motion within the ARF excitation are visualized with high resolution and with relatively deep penetration depth [36-38]. However, ARFI images lack quantitative tissue stiffness information. For SWEI imaging (red and green in Figure 2.1d), shear wave propagation is monitored outside of the ARF excitation region where signal amplitude is lower, but quantitative tissue stiffness information in the form of tissue shear modulus can be derived. First, shear wave group speed (SWS) is extracted from the ensemble of displacement or velocity data using a radon sum transformation [39], cross correlation [40], performing random sample consensus

(RANSAC) [41], or applying machine learning algorithms [42]. From the extracted SWS, assuming the tissue is linear, elastic, isotropic, homogeneous, and incompressible, the Young's modulus, E , can be determined as:

$$E = 3\rho SWS^2 \quad (2.1)$$

where ρ is the tissue mass density [43].

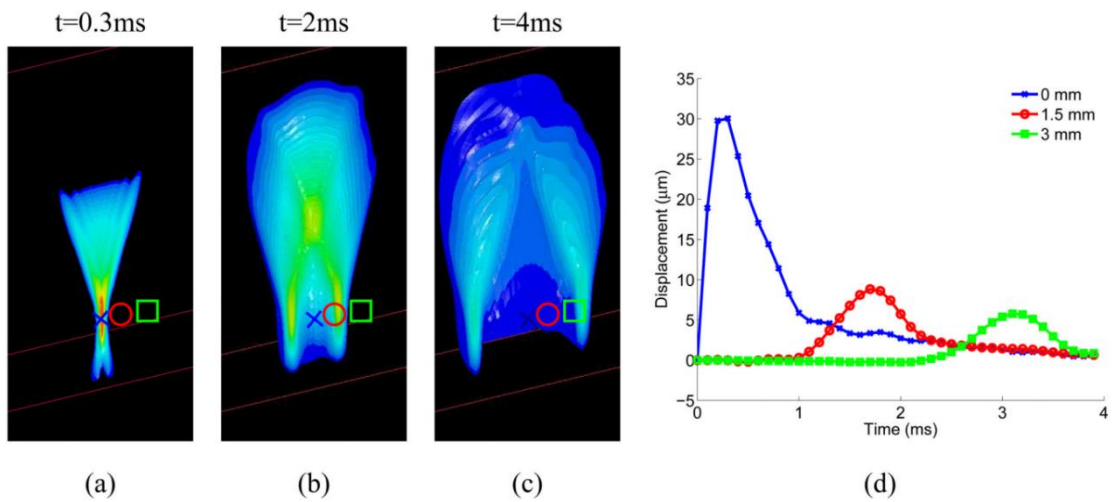


Figure 2.1: A simulated displacement field at different time points after the initial ARF push pulse from a transducer. The transducer face is at the top of the image facing down. Positive displacement is away from the transducer face also straight down. The blue curve in d) is the high-amplitude on-axis displacement that corresponds with information displayed by an ARFI image. The red and green curves in d) are lower-amplitude off-axis displacement data that are needed to determine SWS and to estimate shear modulus. Figure reproduced from [34].

2.1.1 ARF Pushing Pulses

When ultrasound waves propagate through tissue, the attenuation of the tissue absorbs and scatters a portion of the wave energy [44]. A portion of the absorbed wave

energy is transferred into the tissue as momentum which results in an acoustic radiation force (ARF) modeled by:

$$F = \frac{2\alpha I}{c}, \quad (2.2)$$

Where F denotes the generated ARF in $\text{kg}/(\text{s}^2\text{cm}^2)$, α represents the tissue absorption coefficient in Np/m , I is the pulse average acoustic beam intensity in W/cm^2 , and c is the sound speed in m/s [45]. Even though ARF is generated during all ultrasonic propagation through soft tissue, only high energy and long duration ($> 100 \mu\text{s}$) focused pulses are capable of generating micron scale displacements. In order to keep the ARF impulse-like, the duration of the push excitations needs to be shorter than the dynamic response of tissue ($< 1\text{ms}$) [6]. Per Equation 2.2, the magnitude of the ARF generated for a given tissue attenuation coefficient and sound speed is directly proportional to the pulse average acoustic intensity. Since the pulse average acoustic intensity is directly related to the square of the pressure amplitude, using higher pressure amplitude push transmit pulses increases ARF and therefore tissue displacement for a given push transmit duration.

2.1.2 Tracking Pulse Approaches

Following an ARFI push, shear waves are generated perpendicular to the original push direction (Figure 2.1a-c). The motion generated by the resulting shear waves can be imaged using repeated tracking pulses transmitted in an ensemble over a

lateral span outside the push excitation region (Figure 2.2). Ultrasonic motion estimation techniques are then applied to quantify the dynamic tissue response.

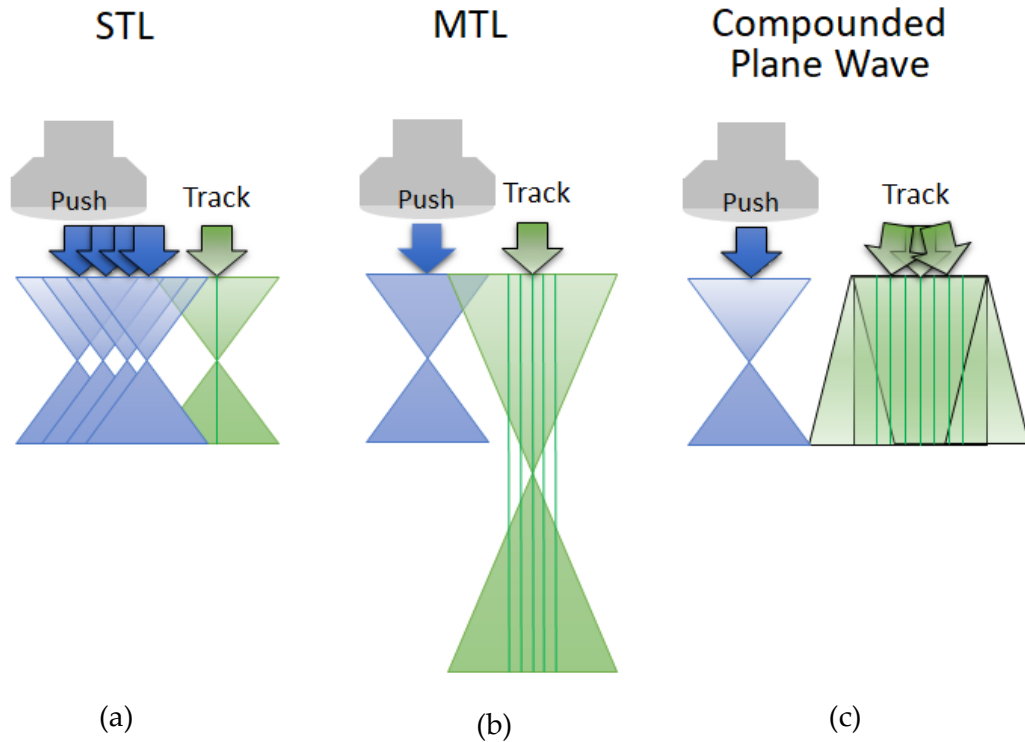


Figure 2.2: Three types of shear wave tracking configurations. (a) STL uses a single-track beam location to track shear wave propagation generated from multiple ARF pushes at varying lateral distances away [29]. (b) MTL uses a single push and track location pair. The track beam is focused deep to the push focus and less tightly compared to the STL track beam, and multiple lateral track lines are derived from a single track transmit [30, 46]. (c) Compounded plane wave tracking also uses a single push beam, but it coherently sums the multiple angled plane wave track transmits to form lateral track lines encompassing the widest lateral field of view [47].

As shown in Figure 2.2 a-c, there are 3 track pulse focal configurations that have been employed in SWEI imaging: 1) single track location (STL) [29, 30], 2) multiple track location (MTL) [46], and 3) plane wave [47]. STL repeatedly uses a single tightly focused

transmit tracking beam configuration combined with multiple ARFI pushes at increasing lateral positions to acquire a single SWEI measurement. From the single and tight tracking transmit focus employed with this method, STL benefits by having reduced speckle bias, but STL is slow to acquire data and increases energy deposition in the body due to the use of multiple ARFI pushes for a single acquisition. Due to these drawbacks, MTL and plane wave, coherently compounded tracking beams are preferentially implemented commercially for SWEI [35]. These methods monitor shear wave propagation across a 2D field of view from a single push pulse. MTL repeatedly uses a single weakly focused transmit beam to track a single ARFI push over a finite field of view while plane wave imaging removes the transmit focusing all together. Because MTL retains some focusing on transmit, it benefits from increased signal strength as compared to plane wave, however, the shear wave is typically monitored over a smaller field of view with MTL.

Pulse inversion tissue harmonic imaging (THI) has been applied to SWE tracking [48]. As with THI B-mode, harmonic SWE tracking reduces reverberation clutter, off-axis scattering, and phase aberration when estimating tissue motion [24, 49], which leads to improved tracking data quality [23] and has been shown to improve SWE measurement success in human livers [50]. Additionally, harmonic SWE tracking has been shown to reduce displacement underestimation bias by decreasing track beamwidth [24, 48]. However, as with B-mode, harmonic SWE tracking suffers from lower electronic SNR

compared to the fundamental signal [27]. Lower SNR increases displacement estimation uncertainty (i.e., jitter), which is predicted by the Cramér-Rao lower bound (CRLB) [51]:

$$Jitter \geq \sqrt{\frac{3}{2f_c^3 \pi^2 T (BW^3 + 12BW)} \left(\frac{1}{CC^2} \left(1 + \frac{1}{SNR} \right)^2 - 1 \right)} \quad (2.3)$$

where f_c is the center frequency, T is the correlation window length in seconds, BW is the fractional bandwidth, CC is the signal correlation coefficient, and SNR is the electronic signal-to-noise ratio.

2.2 Mechanical Index (MI)

The FDA established the MI as an acoustic output metric to address the potential risks of non-thermal mechanical effects during diagnostic ultrasound exams in 1992 [25, 26, 33]. Its formulation is based upon observations of acoustic cavitation in the presence of optimally-sized gas bubbles in water [52, 53], and it is defined as:

$$MI = \frac{p_{r0.3}(Z_{MI})}{\sqrt{f_{awf}}} \quad (2.4)$$

where $p_{r0.3}(Z_{MI})$ is the attenuated (derated) peak-rarefactional acoustic pressure at the depth Z_{MI} (assuming an attenuation coefficient $\alpha = 0.3\text{dB/cm/MHz}$); Z_{MI} is depth on the beam axis from the transducer to the plane of maximum attenuated pulse-intensity integral (which generally occurs near the shallower focal depth when the electronic lateral focus differs from the elevational lens focus), and f_{awf} is the acoustic-working frequency.

The FDA adopted an MI threshold guideline of 1.9 because this value corresponds to the maximum MI that was computed for ultrasound scanners in use prior to 1976 when the FDA began monitoring acoustic output, and, no deleterious events had been reported for ultrasonic imaging prior to 1976 [54]. The MI is commonly further limited by commercial ultrasound vendors when a 20-30% safety buffer is applied to reduce the number of production transducers requiring quality assurance testing [27, 28], which results in most current commercial scanners using a maximum MI between 1.3 and 1.6.

2.3 Tissue Harmonic Imaging (THI)

Initially used with ultrasound contrast agents to distinguish against other background echoes, harmonic imaging uses a broadband transducer to transmit at frequencies below its center frequency for transmit and then listens for echoes at the second harmonic of the transmit frequency [21]. Tissue Harmonic Imaging (THI) was later found to work in tissue without contrast agents and to provide better image quality than conventional fundamental frequency images [9]. As a result, the current default imaging mode for hepatic ultrasound is THI [15, 16, 55, 56]. Instead of the original bandwidth-limited filtered harmonic signals [57], pulse inversion (PI) sequences where sequential inverted pulses of positive and negative leading edges (180 degrees out of phase) are summed to remove the fundamental frequency and the odd harmonics are

used today [9]. Higher odd harmonics can be ignored in practice due to the limitations of modern transducer bandwidth.

THI generally forms images with reduced acoustic clutter compared to conventional fundamental imaging. This is due to the harmonic signal being generated near the focal depth, bypassing aberrating and reverberating pre-focal structures and reducing reverberation clutter and sidelobe levels [9, 23, 24]. THI signals, however, are susceptible to low SNR because they are the product of nonlinear wave propagation [9, 27]. In commercial ultrasound scanners, the resulting THI signals from nonlinear propagation are generally 15-20 dB lower in amplitude than the corresponding fundamental signals [22].

In the case of plane wave imaging, there is no transmit focusing. Since harmonic signal generation increases quadratically with source pressures, plane wave harmonic imaging does not benefit from bypassing the pre-focal aberrating and clutter generating structures. As such, the work presented in this thesis will focus on focused transmitted harmonic pulses.

2.4 Spatial Coherence

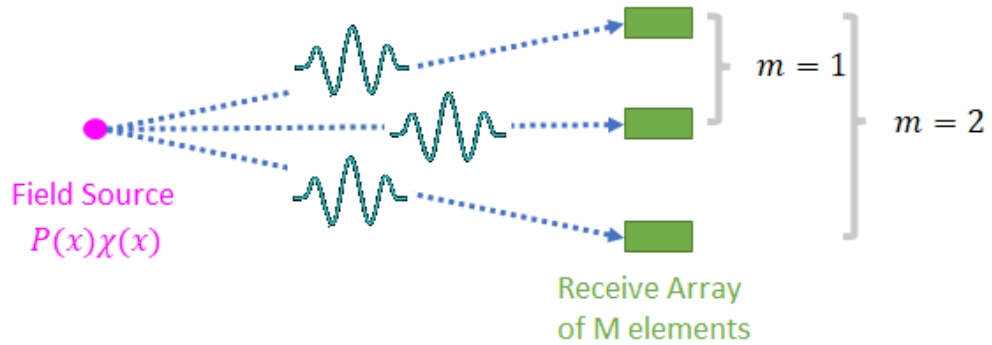


Figure 2.3: Reflected ultrasonic pulse signal from a point in the imaging field to 3 elements on a transducer array used to calculate spatial coherence. Correlation between time delayed signals from adjacent elements represent coherence at lag 1 ($m = 1$). Correlation between elements spaced one element apart are coherence at lag 2 ($m = 2$).

Spatial coherence is the measure of similarity between signals at separate locations in space. In the field of diagnostic ultrasound, this can be interpreted as a measure of correlation between time-delayed channel signals as a function of their channel spacing or lag visualized in Figure 2.3. Mallart and Fink showed that the van Cittert-Zernike (VCZ) theorem [58, 59] can be used to predict the spatial coherence of an incoherent speckle source as the Fourier transform of the source intensity [60] as shown in Equation 2.5. $R(m)$ refers to the normalized correlation value at lag m , $R'(0)$ is the correlation at lag = 0 used to normalize the correlation, $P(x)$ is the pressure in the field at the lateral position x , and $\chi(x)$ is the reflectivity in the field at the lateral position x . In

the presence of fully developed speckle, $\chi(x) = 1$ because reflectivity is uniform, and Equation 2.5 simplifies to Equation 2.6.

$$R(m) = \frac{1}{R'(0)} FT\{|P(x)\chi(x)|^2\} \quad (2.5)$$

$$R(m) = \frac{1}{R'(0)} FT\{|P(x)|^2\} = \frac{1}{R'(0)} FT\{P(x)P^*(x)\} \quad (2.6)$$

Using the Fresnel diffraction assumption, we can express $P(x)$ as the Fourier transform of $A(x')$, the transmit aperture function where x' is the lateral position on the aperture. Replacing pressure in the right-hand side of Equation 2.6 with the aperture function, we can express the spatial coherence as a function of the transmit aperture using Equation 2.7.

$$R(m) \propto A(-x') * A(x') \quad (2.7)$$

2.5 Acoustic Clutter

Acoustic clutter can decrease the pressure reaching the focus. Acoustic clutter causing focal energy loss can be categorized into 2 types: 1) phase aberration, and 2) reverberation clutter. Phase aberration is the distortion of the wave front and focal profile during propagation through heterogeneous sound speed material. Reverberation clutter refers to ultrasound signals that have been multiply-reflected which do not reach the focus.

Spatial coherence is sensitive to all forms of acoustic clutter. For phase aberration, the changes in coherence can be modeled by Eq. 7 [51], where $R_{vcz}(m)$ is the

coherence of the ideal noise-free VCZ case, $e^{-(2\pi f_0)^2(R_{\tau\tau}(0) - R_{\tau\tau}(m))}$ represents the distortion from phase aberration, f_0 denotes the transmit frequency, and $R_{\tau\tau}(m)$ is the spatial autocorrelation of aberration profile.

$$R(m) = R_{VCZ}(m)e^{-(2\pi f_0)^2(R_{\tau\tau}(0) - R_{\tau\tau}(m))} \quad (2.8)$$

Reverberation clutter can be modeled as spatially uncorrelated signals. If the signal is completely spatially uncorrelated, autocorrelation at lag 0 would remain 1 while correlation at all other lags would be 0. This coherence profile would be represented with Eq. 8, a delta function at lag $m = 0$.

$$R(m) = \begin{cases} 1, & m = 0 \\ 0, & m \neq 0 \end{cases} \quad (2.9)$$

Generalizing Eq.8 for all levels of reverberation clutter relative to the channel signal results in Eq. 9, which models reverberation clutter as a weighted average of a triangle function and a delta function at lag 0 [61, 62]. The decrease after lag one is scaled by the clutter noise to signal ratio (NSR).

$$R(m) = \begin{cases} 1, & m = 0 \\ \frac{R_{VCZ}(m)}{1 + NSR}, & m \neq 0 \end{cases} \quad (2.10)$$

Chapter 5 leverages the fact that clutter causes decreases in both focal pressures and spatial coherence to relate spatial coherence directly to *in situ* pressure.

3 Quantifying the Impact of Imaging through Body Walls on Shear Wave Elasticity Measurements

This chapter will be submitted for publication to the Ultrasound in Medicine & Biology journal under the same title. It is coauthored with Nick Bottenus, Felix Jin, and Kathryn R Nightingale.

3.1 Introduction

Liver biopsy is a gold standard for staging liver fibrosis [63-65], but its invasive nature and lack of sensitivity [66-68] decrease its utility as a diagnostic tool for longitudinal monitoring. Shear wave elasticity imaging (SWEI) [7], a noninvasive diagnostic ultrasound technique that quantifies tissue stiffness, has found success in liver fibrosis staging [70-73].

SWEI uses acoustic radiation force impulse (ARFI) excitations from an ultrasound transducer to induce localized tissue displacement (i.e., to push tissue) at depth [7]. Equation 3.1 describes the acoustic radiation force (ARF), F , generated by an ARFI excitation [6]. In the equation, α represents the tissue acoustic absorption, I denotes the pulse averaged acoustic beam intensity, and c is the speed of sound in the tissue of interest. The tissue particle motion induced by the ARFI push and subsequent shear wave propagation is then tracked using the same transducer with standard ultrasonic tissue motion estimation methods to determine the shear wave speed (SWS) [7]. Assuming the tissue is linear, elastic, isotropic, homogeneous, and incompressible,

Equation 3.2 details the relationship between the estimated Young's modulus, E , and the SWS, where ρ is the tissue mass density [74].

$$F = \frac{2\alpha l}{c} \quad (3.1)$$

$$E = 3\rho SWS^2 \quad (3.2)$$

During clinical application, studies have reported SWEI acquisition failures and unreliable SWS measurements in patients with elevated body mass index (BMI) and for some subjects with advanced hepatic fibrosis [14-19]. Because SWEI sequences consist of two distinct operations (pushing and tracking), acquisition failures have been attributed to (1) insufficient ARF generation resulting in inadequate tissue particle motion amplitude, and/or (2) distorted ultrasonic tissue motion tracking. Previous studies have demonstrated significantly decreased ARFI push amplitude *in situ* through some body walls as compared to phantoms [28, 75]. Preliminary studies have also demonstrated that body wall distortion of the tracking beams decreases shear wave elasticity (SWE) measurement success [27]. The use of elevated transmit pressures and therefore elevated mechanical index (MI) [54] ($1.9 < MI < 3.5$) for pushing and/or harmonic tracking beams has been demonstrated to improve SWE measurement success [27, 28]. However, it remains unclear which of the two SWEI sequence operations is more impacted by the presence of body walls and if one of them might preferentially benefit from the use of elevated MI transmit pulse configurations.

Additionally, previous studies that reported improved SWE measurement success when using elevated MI for harmonic tracking only explored using single track location-SWEI (STL-SWEI) [27]. STL-SWEI repeatedly uses a single tightly focused harmonic transmit tracking beam configuration combined with a series of ARFI pushes at increasing lateral distance from the track beam to acquire a single SWE measurement [29, 30]. From the tight transmit/receive focus of the tracking beam, STL-SWEI benefits from optimal focusing and reduced speckle bias [29, 46], but is slow to acquire data due to the use of multiple ARFI pushes for a single acquisition. In lieu of STL-SWEI, parallel receive multiple track location-SWEI (MTL-SWEI) [35] is often used commercially. MTL-SWEI uses either plane-wave or weakly focused transmit track beams to image the tissue response to a single ARFI push. Although the defocused MTL tracking beam configurations are more susceptible to speckle bias as compared to STL, MTL-SWEI sequences are much faster than their STL counterparts because they require only a single push per acquisition. Therefore, an additional goal of this work is to extend our prior observations on SWEI measurement success with elevated MI tracking in STL-SWEI to MTL-SWEI.

Herein, we built an opposing window experimental setup that separately isolated body wall effects between the push and track SWEI operations. Additionally, instead of using the STL-SWEI tracking configuration of the previous study [27], we examined MTL-SWEI track sequences. We independently assessed the effects of body

walls on the pushing and tracking operations of SWEI as a function of MI, spanning 5 different push beam MIs and 10 track beam MIs.

3.2 Methods

As shown in Figure 3.1, two opposing, synchronized transducers were used in tandem: an abdominal imaging DAX transducer array (transducer one, 1.6 MHz center frequency) on a commercial imaging system (Sequoia, Siemens Medical Solutions, Issaquah, WA, USA), and an L7-4 transducer (transducer two, 5.2 MHz center frequency) on a research platform (Vantage 256, Verasonics, Kirkland, WA, USA). The relative positioning of the two transducers had the Sequoia commercial system imaging through body walls to best represent clinical abdominal imaging and the Verasonics system bypassing body walls to provide control reference measurements. We used three imaging combinations as shown in Figure 3.1 and Table 3.1: 1) push and track through body wall with transducer one, 2) push through body wall with transducer one and track without the body wall with transducer two, and 3) push without the body wall with transducer two and track through body wall with transducer one.

3.2.1 Transducer and System Configuration

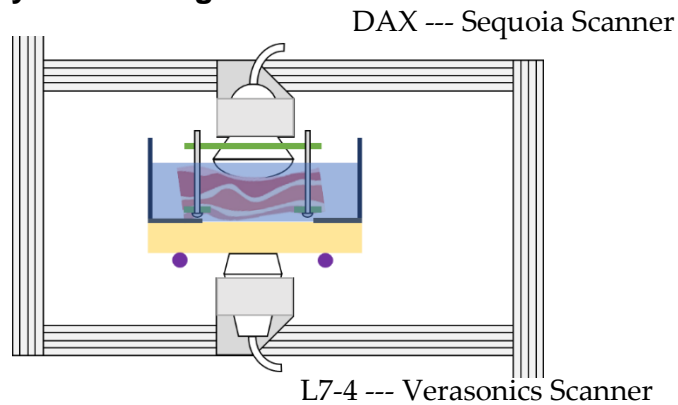


Figure 3.1: Opposing window experimental setup. DAX transducer was on top imaging the homogeneous liver speckle phantom through body wall samples while submerged in attenuating fluid. L7-4 transducer was placed below and aligned with the same imaging plane using custom transducer holders attached to a rigid aluminum rectangular frame.

Table 3.1: 3 combinations of transducers used for push and track sequences in the opposing window experimental setup. Since body wall samples are always secured to the DAX transducer, the DAX always pushes/tracks through body walls. Since the L7-4 is directly imaging into the liver phantom, the L7-4 always pushes/tracks without a body wall.

SWE Imaging Configuration	Push Transducer	Track Transducer
1	DAX	DAX
2	DAX	L7-4
3	L7-4	DAX

The DAX transducer, operated using the Siemens Sequoia scanner, was secured to a rigid aluminum frame using a custom quick-release transducer holder in a downward imaging position. Opposing the DAX transducer and in the same imaging plane, the L7-4 transducer, operated using the Vantage 256 scanner, was also secured to the frame using a custom transducer holder in an upward orientation. The vertical

distance between the two transducer faces was 85 mm. The bottom L7-4 transducer imaged into a stiff (5.13 m/s, 79 KPa) liver mimicking elasticity phantom (Computerized Imaging Reference Systems, Norfolk, VA, USA) through a thin layer of ultrasonic scanning gel (Clear Image Singles, NEXT Medical Products Company, Branchburg, NJ, USA). The phantom was removed from its original protective case to allow for imaging from both sides. To minimize precompression from the weight of the phantom on the L7-4 transducer face, a ring stand was used to support and hold the phantom in place. On top of the liver phantom, a tray with a Tegaderm membrane (Model 1626W, 3M, Saint Paul, MN, USA) cut-out window was used to hold a solution of evaporated milk and saline tuned to a sound speed of 1540 m/s and acoustic attenuation coefficient of 0.5 dB/MHz/cm as coupling media [77-79]. A thin layer of water (<1 mm) coupled the Tegaderm membrane to the liver phantom. Submerged in the evaporated milk coupling media, the DAX transducer imaged through fresh pork belly sections, sourced from the local grocery store, at room temperature after degassing to mimic human abdominal walls [78, 79]. Herein, the pork belly sections will be referred to as body walls. To simulate the pressing of the transducer into the human abdominal wall done during clinical imaging, 3-D printed clamps, which did not obstruct the imaging window, were used to push the body walls against the DAX transducer face.

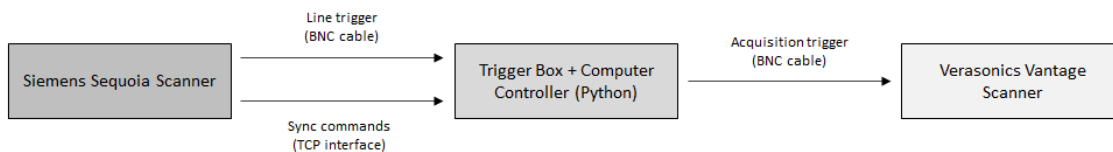


Figure 3.2: Control diagram for one-way synchronization from Sequoia system to Vantage system. For a given transmit condition, two signal streams were output from the Sequoia scanner to an intermediary computer with triggering control. One output was a line trigger via BNC cable while the other was a synchronization gating command via an ethernet cable. The combination of line trigger signals and gating signals were combined by the intermediary control computer to output a single acquisition trigger input signal for the Vantage system via BNC cable.

Synchronization between the two scanners followed the diagram in Figure 3.2. In addition to the native line trigger output from the Sequoia scanner, a slower gating command via Ethernet cable using a TCP interface was used to isolate the trigger corresponding to the beginning of the SWE sequence. The custom-built intermediary trigger box and computer controller combined the two Sequoia control signals and generated a trigger signal for the Verasonics scanner to synchronize data acquisition between the two scanners.

3.2.2 SWEI Data Acquisition

Table 3.2: Push pulse parameters for the DAX and L7-4 transducers which were selected to generate similar push displacement amplitudes in the phantom from each transducer.

Push Sequence Parameters	DAX	L7-4
Transmit Frequency [MHz]	2.2	4
Focal Depth [mm]	64	25
Lateral F/#	1.6	2
Push Cycles	400	790

Push Displacement [μm]	2.3	2.3
Default MI	2.3	2.5

Table 3.3: SWEI tracking parameters for the DAX and L7-4 transducers.

Track Sequence Parameters	DAX	L7-4
Tx Frequency [MHz]	1.3	5.2
Tx Focal Configuration	Deep Focal Depth	Plane Wave
Rx Frequency Configuration	ALP Harmonic	Fundamental
# Parallel Receive Beams	32	136
Lateral FOV [mm]	9.56	19.96
PRF [KHz]	5	10
Pulse Duration [cycles]	1.25	1

3.2.2.1 DAX Push and Track (Table 3.1: Imaging Combination 1)

When examining the effects of changing MI for ARFI push and SWEI track while imaging through body walls, only the DAX transducer was used and the L7-4 transducer was turned off such that both the push and track signals propagated through the body walls. The DAX push parameters shown in Table 3.2 were selected to match a previous study [27]. When varying push MI, push duration was held constant, thus the total energy deposited increased with increasing MI. The following 5 push MI values were used for the DAX transducer: 1.1, 1.5, 1.7, 2.1, and 2.3. Track transmit parameters used by the DAX are shown in Table 3.3. Fully sampled Alternating Line Phase (ALP) pulse inversion (PI) [80] was used to recover harmonic 2.6 MHz center frequency data. For the tracking sequence described, the track MI was varied 10 times corresponding to

the following values: 0.2, 0.3, 0.5, 0.8, 1.0, 1.2, 1.3, 1.4, and 1.5. The upper limit of the track transmit MI was limited by the scanner software and focal depth. When varying pushing MI, the DAX tracking MI was held at the maximum value of 1.5. When varying tracking MI, the DAX push MI was kept at 2.3. Each acquisition was repeated 5 times with the same speckle realization to characterize scanner repeatability. A total of 28 body walls ranging between 1.8 cm and 4.1 cm thick were imaged.

3.2.2.2 DAX Push with L7-4 Track (Table 3.1: Imaging Combination 2)

When isolating the effects of body wall on only the push, DAX tracking was turned off and the L7-4 track sequence was turned on. The L7-4 track transmit parameters used are displayed in Table 3.3. L7-4 tracking did not use harmonic, angular compounding, or transmit focusing because it was imaging directly into the liver mimicking phantom which is a straightforward imaging situation without aberration or clutter generating structures. All 5 DAX push MIs used in imaging combination 1 shown in Table 3.2 were collected for imaging combination 2 for same set of 28 porcine body walls. For each push transmit configuration and each body wall, 5 repeat acquisitions were collected.

3.2.2.3 L7-4 Push with DAX Track (Table 3.1: Imaging Combination 3)

When isolating the effects of body wall on only the track, the DAX tracking configuration was used with the L7-4 push configuration. The L7-4 push parameters are shown in Table 3.2. This matched the peak displacement generated by the DAX at a

magnitude of 2.3 μm at the same imaging depth plane in the phantom. The 10 DAX track MIs used in imaging combination 1 shown in Table 3.3 were collected for all 28 porcine body walls for imaging combination 3. For each track transmit configuration on each body wall, 5 repeat acquisitions were collected.

3.2.3 Spatial Coherence Data Acquisition

Harmonic lag one coherence (LOC) [62] and harmonic short-lag spatial coherence (HSC) [81] are evaluated herein. LOC has previously been shown to increase with increasing transmit pressure until a plateau with sufficient electronic SNR [62]. HSC has previously been shown to strongly correlate with B-mode *in situ* peak pressures. Since it was not possible to measure peak *in situ* pressures directly for each body wall, peak *in situ* on-axis focal displacement amplitude from an ARFI push pulse was used as a proxy measurement for peak *in situ* pressure. *In situ* peak displacement is a function of the time average intensity of the *in situ* acoustic beam (Equation 3.1) and scales with the square of *in situ* pressure. *In situ* peak displacement amplitude was quantified with the Verasonics system (no body wall). HSC and LOC were computed using pulse inversion B-mode channel data collected using the DAX transducer imaging through the body walls and the Sequoia scanner matching the push transmit beam focal configuration with those used during the corresponding the SWEI data acquisition. From the center 11 B-mode lines, harmonic spatial coherence was computed from which HSC and LOC were extracted.

3.2.4 SWS Estimation

Standard SWEI data processing methods were implemented [27, 28]. Briefly, tissue particle velocity was determined using a progressive-reference phase shift estimator, Kasai algorithm [92], on beamformed in-phase and quadrature (IQ) data. The same processing code was used for data from each system. An axial averaging kernel size of 6 track beam wavelengths was applied to suppress noise. Additionally, a low pass filter with cutoff frequency at 1000 Hz was applied to the tissue velocity data to simulate clinical data processing [27]. Velocity data within the push beam's axial depth of field (DOF - 9.45 mm for the DAX, 9.24 mm for the L7-4) was compressed using the axial mean. The mean shear wave tissue velocity across the lateral field of view was then assessed using a Radon Sum/LatSum algorithm to estimate SWS [39]. Each SWS measurement corresponding to each repeated acquisition was considered successful if the estimated SWS was within 10% of the ground truth SWS (5.13 m/s), which was measured in the phantom without a body wall using all imaging configurations. In addition to the LatSum method, another SWS estimation technique, SweiNet [42], was also applied to the entire dataset. SweiNet has been shown to give consistent SWS results to LatSum, and in addition it provides an uncertainty metric for every estimate – with noisy data generating larger uncertainty.

3.2.5 Peak Displacement and Jitter Estimation

From the L7-4 tracked data collected after pushing with the DAX, point displacements were estimated using the same Kasai algorithm [82] along with an axial averaging kernel of 6 track beam wavelengths. To compute the on-axis peak displacement, point displacements spanning 2 mm laterally centered around the push focus and 9.24 mm axially (the axial DOF) were averaged.

To compute the displacement estimation jitter magnitude, point displacements were computed for the reference track frames before the push, where there was no actual motion. These displacements were averaged over the DOF of the push beam. Jitter magnitude was then determined by taking the standard deviation of two consecutive frames [51].

3.2.6 MI Measurement

After completing 3D scans using a computer-controlled three-axis translation stage (MM3000, Newport Corporation, Irvine, CA, USA) in a deionized (DI) water tank, peak intensity pressure signals for each transmit configuration were recorded using an Acertara 804 polyvinylidene fluoride (PVDF) membrane hydrophone (Acertara Acoustic Laboratories, Longmont, CO, USA) and a LeCroy Wavesurfer MXs-B oscilloscope (Teledyne LeCroy, Chestnut Ridge, NY, USA). The output voltage waveforms from the membrane hydrophone were then converted to pressures using magnitude deconvolution [83], where the frequency-dependent magnitude sensitivity of the

hydrophone was accounted for using an 1-20 MHz calibration. MI was then computed from the derated peak rarefactional pressure per AIUM/FDA guidelines [25, 26, 33, 84].

3.3 Results

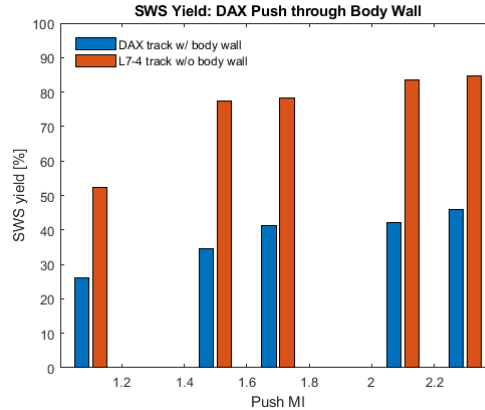


Figure 3.3: Percentage yield of successful SWS measurements as a function of ARFI push beam MI from acquisitions for all 28 body walls. (Blue) Results from imaging combination 1 acquisitions where the DAX transducer was used for both push and track pulses through body walls. (Red) Results from imaging combination 2, where the DAX pushed and the L74 tracked.

Figure 3.3 plots the percentage of successful SWS measurements as a function of DAX transducer push MI. For both the DAX tracked and L7-4 tracked data, the SWS yield increases monotonically with increasing DAX push MI. When tracking with the L7-4, bypassing body walls, SWS yield increased between 26% and 42% compared to when tracking with the DAX through body walls. Still, tracking without body walls using the L7-4 at the maximum DAX push MI of 2.3 yielded 16% unsuccessful measurements highlighting the presence of cases where not enough energy was

deposited through the body walls to generate a measurable shear wave even with ideal tracking.

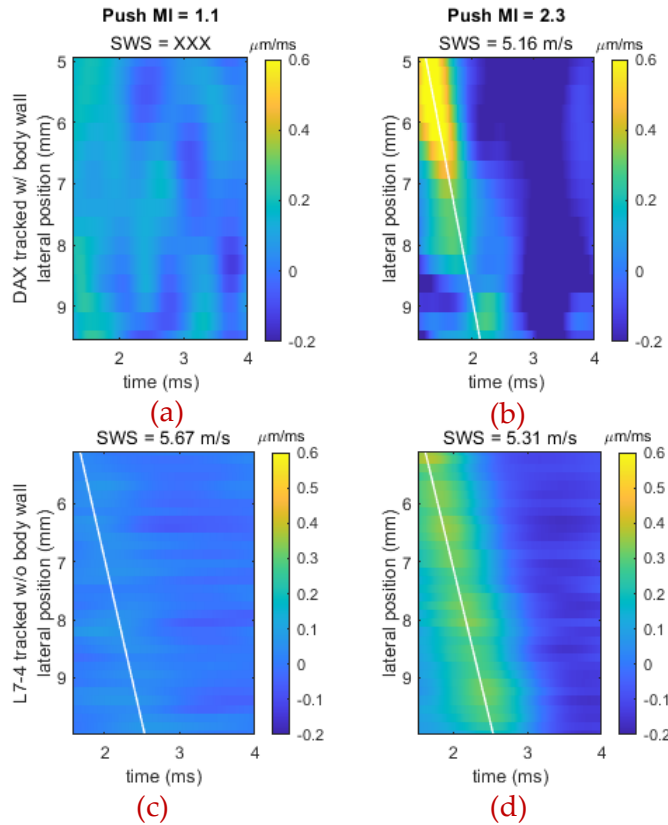


Figure 3.4: Sample shear wave trajectories from acquisitions from varying push MI in one body wall. Left column corresponds to push MI of 1.1. Right column corresponds to push MI of 2.3. Top row contains velocity data tracked through the sample body wall using the DAX (imaging combination 1). Bottom row displays corresponding L7-4 tracked velocity data (imaging combination 2).

Figure 3.4 a-d illustrates sample velocity-based shear wave trajectories from a single body wall. When tracking with the DAX through the body wall and pushing with the DAX (imaging combination 1) at an MI of 1.1, no shear wave propagation was observed (Figure 3.4a). Increasing the push MI to 2.3 resulted in a successful SWS measurement of 5.16 m/s (Figure 3.4b) with the DAX. When lowering the push MI back

down to 1.1 and using the L7-4 for tracking (imaging combination 2), shear wave propagation was observed (Figure 3.4c). This SWS, however, did not qualify as a successful SWS measurement because the 5.67 m/s SWS was more than 10% greater than the ground truth. Using a high push MI of 2.3 from the DAX and tracking without the body wall with the L7-4 (imaging combination 2) resulted in a successful SWS measurement with an estimate of 5.31 m/s (Figure 3.4d). Figure 3.4c illustrates the increased sensitivity to small velocities when bypassing the body wall by tracking with the L7-4.

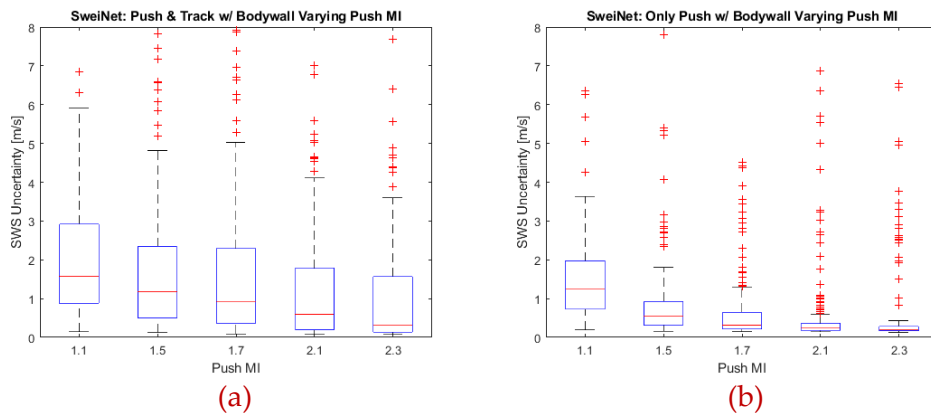


Figure 3.5: SweiNet SWS uncertainty as function of push MI when using imaging combination 1 (pushing and tracking through body walls) in (a). SweiNet SWS uncertainty as function of push MI when using imaging combination 2 (pushing through body walls and tracking without body walls) in (b).

Figure 3.5 shows trends of decreasing SWS estimation uncertainty with increasing push MI for both imaging combinations (tracking with (Figure 3.5a) or without (Figure 3.5b) body walls). As expected, tracking without body walls also decreased the SWS uncertainty at every MI measured compared to tracking through the body walls.

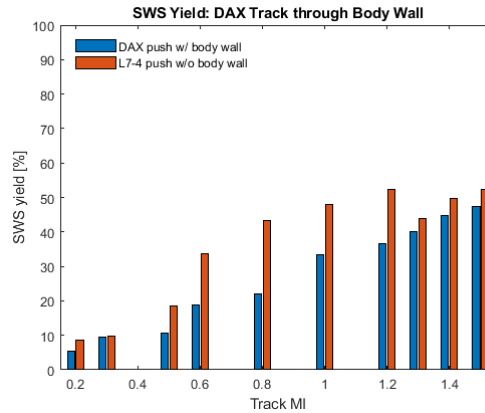


Figure 3.6: Percentage yield of successful SWS measurements as the DAX harmonic SWE track pulse MI increased from 0.2 to 1.5 across acquisitions for all 28 body walls. (blue) Results from imaging combination 1 acquisitions where the DAX transducer was used for both push and track pulses. (red) Results from imaging combination 3 acquisitions where the DAX transducer was only used for track pulses through the body walls and the L7-4 transducer generated push beams without the body walls.

Figure 3.6 plots the percentage of successful SWS measurements as a function of DAX transducer track MI. SWS yield increased monotonically with DAX track MI when the DAX was used to push through the body walls (imaging combination 1). Pushing with the L7-4, bypassing the body walls for the push (imaging combination 3), resulted in increasing SWS yield with DAX track MI up to a plateau (DAX track MI ~ 0.8). As expected, L7-4 pushing resulted in higher SWS yield than DAX pushing through the body wall at every DAX track MI level examined. The difference in SWS yield between L7-4 pushes (no body walls) and DAX transducer pushes (through body walls) was larger for lower DAX track MIs: 21% for a DAX track MI = 0.8, decreasing to only 4% as DAX track MI increased to 1.3. When pushing through body walls, higher track beam

MIs are needed to achieve the same level of SWS yield by decreasing tracking jitter magnitude in order to compensate for the lower amplitude shear waves.

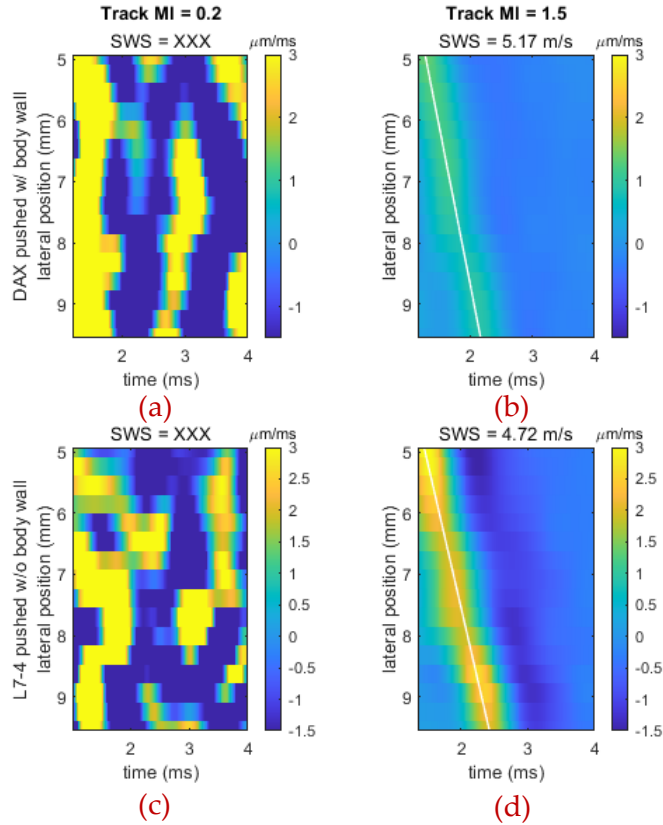


Figure 3.7: Sample shear wave trajectories from acquisitions varying DAX track MI in one body wall. Left column corresponds to DAX track MI of 0.2. Right column corresponds to DAX track MI of 1.5. Top row contains velocity data pushed and tracked through the body wall using the DAX transducer (imaging combination 1). Bottom row displays corresponding data from the same body wall while tracking through the body wall with the DAX but pushing with the L74 bypassing the body wall (imaging combination 3).

Figure 3.7 illustrates sample velocity-based shear wave trajectories from a single body wall for two different track MIs. When pushing with the DAX through the body wall and tracking with the DAX through the body wall (imaging combination 1) with a track MI of 0.2, no shear wave propagation was observed (Figure 3.7a). Increasing the

track MI to 1.5 resulted in a successful SWS measurement of 5.17 m/s (Figure 3.7b) for the same pushing pulse. When lowering the DAX track MI back down to 0.2 and using the L7-4 for pushing (imaging combination 3), shear wave propagation was not observed (Figure 3.7c). However, increasing the DAX track MI to 1.5 resulted in a successful SWS measurement with an estimate of 4.72 m/s (Figure 3.7d).

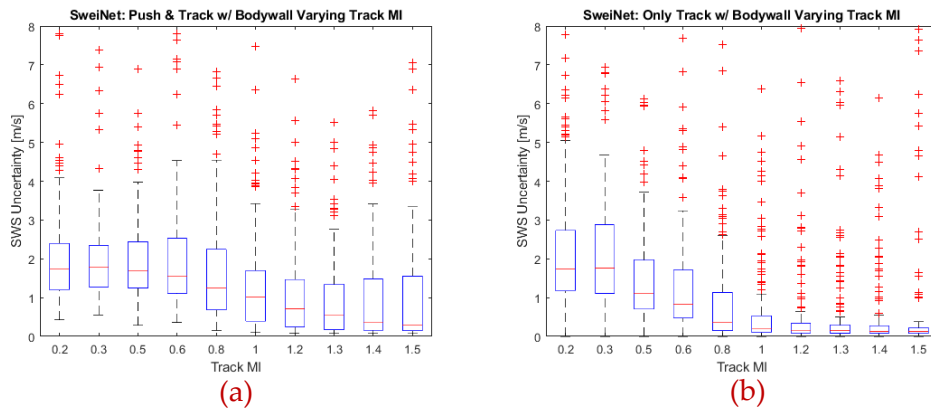


Figure 3.8: SweiNet SWS uncertainty as function of track MI when using imaging combination 1 (push and track through body walls) in (a). SweiNet SWS uncertainty as function of track MI when using imaging combination 3 (push without body walls and track with body walls) in (b).

Figure 3.8 shows trends of decreasing SWS uncertainty with increasing track MI through the body walls when applying SweiNet to estimate SWS for both imaging combinations 1 and 3 regardless of body wall presence during the push transmit. Pushing without the body walls (Figure 3.8b) also decreased the SWS uncertainty at every track MI > 0.5 measured compared to pushing with body walls (Figure 3.8a).

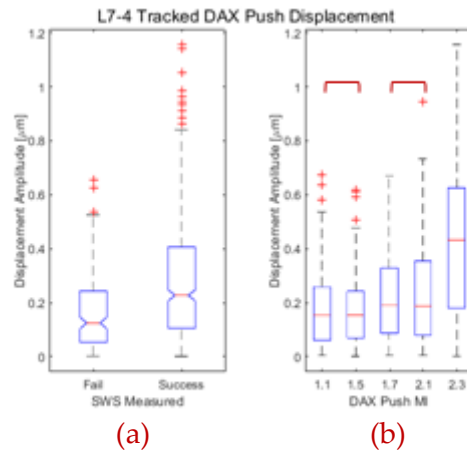


Figure 3.9: Distributions of peak ARFI displacement amplitudes tracked via imaging combination 2 by using the opposing L7-4 to track and the DAX to push through all 28 body walls and all 5 push MIs grouped based on SWS measurement success/failure in (a) showing the range of energy reaching the phantom through the different body walls for a given push configuration. Distributions of peak ARFI displacement amplitudes tracked using the L7-4 for DAX pushes through all 28 body walls as a function of DAX push MI increasing from 1.1 to 2.3 in (b). Note that brackets indicate not significant.

Figure 3.9 plots the distributions of L7-4 tracked peak displacement resulting from DAX pushes through the 28 body walls corresponding to imaging combination 2. The distribution of peak displacement amplitudes from all 5 repetitions, all 5 DAX push MIs, and across all 28 body walls were grouped based on the success or failure of the corresponding SWS estimate in Figure 3.9a. A Wilcoxon rank sum test performed on this binary grouping showed a significant difference of median peak displacement between successful and failed SWS estimates ($p < 0.0001$). When the same data was grouped by push MI in Figure 3.9b, a Kruskal-Wallis test showed that there were significant differences in median peak displacements between different push MIs ($p < 0.05$).

Specifically, Mann-Whitney U-tests demonstrated differences between all combinations of push MIs ($p < 0.05$) except the two combinations in brackets.

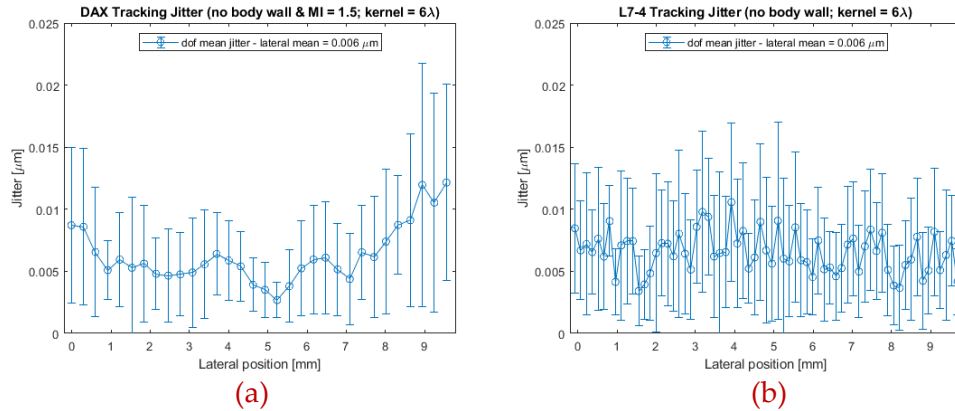


Figure 3.10: Mean and standard deviation of jitter across 15 speckle realizations for each of the 32 parallel receive lines using the DAX transducer at a track transmit MI of 1.5 in (a). Mean and standard deviation of jitter across 15 consecutive frames for each of the plane wave received track lines using the L7-4 transducer as control in (b).

Figure 3.10 examines the displacement estimate jitter magnitudes across the lateral lines for the DAX at the highest track MI of 1.5 and for the L7-4 control case, both without a body wall present. The mean and standard deviation of jitter magnitude were computed from 15 speckle realizations. Mean jitter magnitudes increased at the edge receive lines for the DAX (lateral positions approaching 9mm in Figure 3.10a), unlike the L7-4 in Figure 3.10b, where the mean jitter did not follow a trend across the lateral imaging field. Taking the mean jitter magnitude across the 32 parallel lateral receive lines, however, resulted in the DAX having comparable jitter magnitude to the L7-4 probe across all of the plane-wave parallel receive lines.

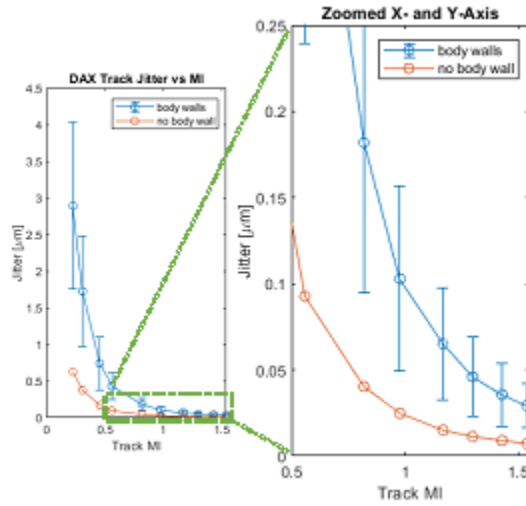


Figure 3.11: Mean track jitter magnitude across the 32 parallel receive lines for the DAX transducer using track MIs from 0.2 to 1.5. Red line represents jitter magnitude when no body walls are present. Blue represents jitter magnitude when body walls are present. Error bars depict median and interquartile range across 28 body walls.

Figure 3.11 investigates the effects of the body wall on the mean jitter magnitude for the DAX transducer as a function of track MI. For a given track MI, inter-body wall median jitter was consistently 4.0 to 4.7 times larger than the no body wall case (using the DAX transducer without an intervening body wall as a reference). The inter-body wall median jitter magnitude at a track MI of 1.5 was larger than the jitter magnitude with no body wall at a track MI of 1.0.

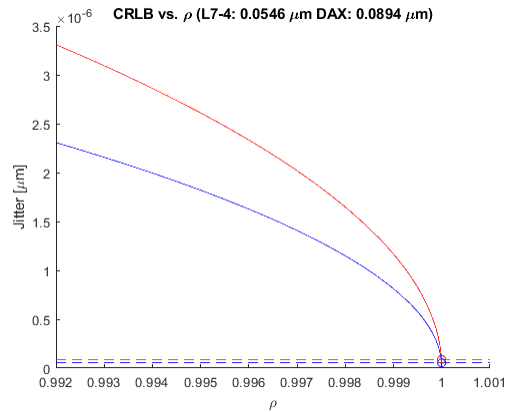


Figure 3.12: Theoretical Cramer-Rao Lower Bound jitter magnitude curves for the DAX and L7-4 transducers as a function of the signal correlation coefficient.

Figure 3.12 depicts the theoretical Cramer-Rao Lower Bound (CRLB) jitter magnitude computed using Equation 2.3 in Chapter 2 [51] for these experiments for both the L7-4 and the DAX. The L7-4 transducer parameters included: 5.2 MHz center frequency, 0.8 fractional bandwidth, 0.192 us window length, and 60 dB SNR. The experimentally measured cross correlation coefficient was 0.999996 which corresponded to a CRLB value of 0.0546 um. For the DAX transducer given 2.6 MHz center frequency, 0.8 fractional bandwidth, 0.75 us window length, 60 dB SNR, and experimentally measured correlation coefficient 0.999995, the corresponding CRLB magnitude of 0.0894 um was computed.

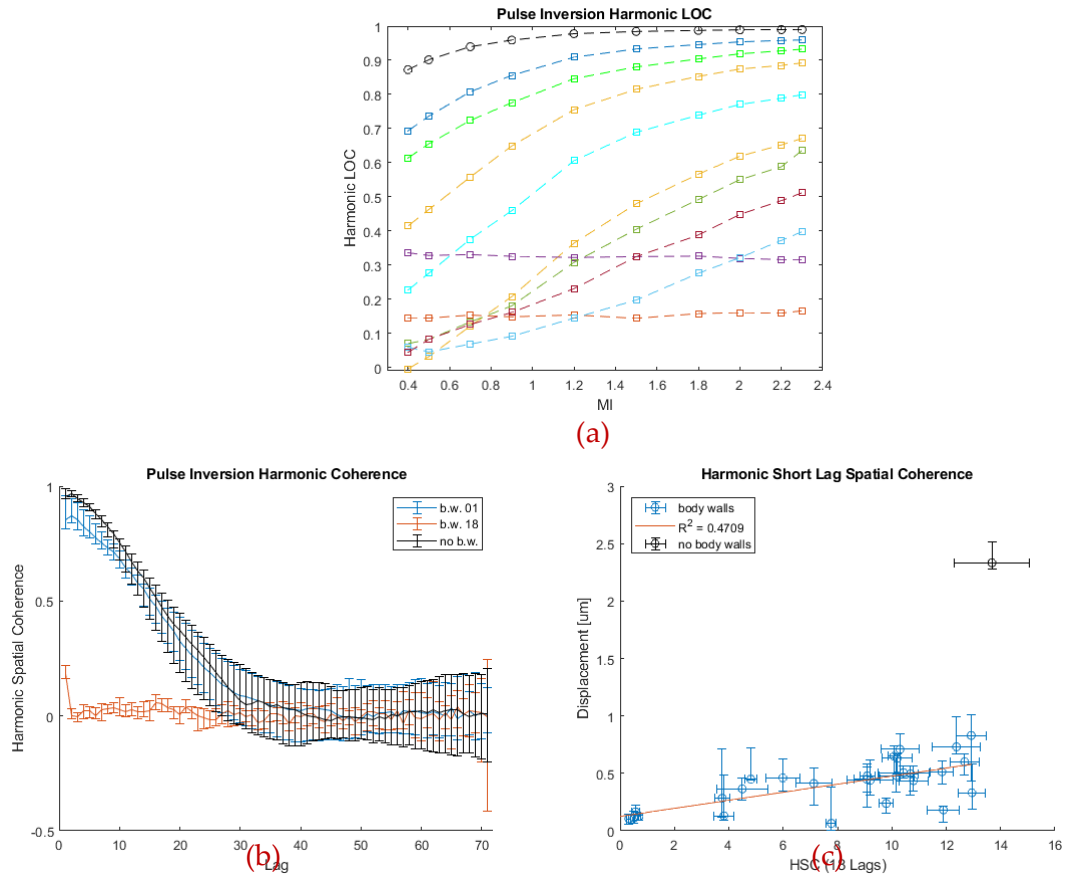


Figure 3.13: Harmonic spatial coherence.(a) Pulse inversion derived second harmonic Lag One Coherence (LOC) in 10 sample body walls(squares) and 1 control sample without a body wall (black circles) as a function of increasing MI from 0.4 to 2.3. (b) Sample second harmonic spatial coherence curves as function of lag for the no body wall control (black), a body wall with high spatial coherence (blue), and a body wall with low spatial coherence (red). The error bars represent the median and interquartile range of 11 overlapping transmit beams. The three colors represent the same samples between plots (a) and (b). (c) Linear regression line between the Harmonic Short Lag Spatial Coherence (HSC) values and ARFI peak displacement values for the 28 body walls (red). X-axis values and error bars represent the median and interquartile range of 11 overlapping transmit beams for HSC. The y-axis values and error bars represent the median and interquartile range across 5 repeated acquisitions for ARFI peak displacements tracked by the L7-4 transducer for DAX pushes at MI = 2.3.

Figure 3.13 illustrates spatial coherence derived image quality metrics obtained when imaging through the body walls in the experiment. Second harmonic LOC, an image quality metric for B-mode [62], was plotted as a function of increasing MI for 10 body walls and the no body wall control (Figure 3.13a). The MI at which the LOC plateaus has been shown to quantify the minimum MI needed to achieve optimal B-mode image quality [62]. Harmonic LOC plateaued at an MI of 1.2 without a body wall while most body walls plateaued at higher MIs. The two exceptions were body walls with exceedingly low LOC that do not change with MI. These two body walls also never yielded successful SWS measurements when pushing and tracking through them. An additional 4 body walls shown in Figure 3.13a exhibited linearly increasing LOC even at a transmit MI of 2.3, suggesting further increases in MI could further improve image quality. The entire spatial coherence curve at MI = 2.3 was plotted for 3 samples in Figure 3.13b. The sample with the highest spatial coherence curve was the control, while the sample just below it was the body wall sample with high LOC (0.95). With the lowest LOC (0.17), the third body wall sample shown in this plot also had the lowest spatial coherence curve. Finally, the HSC [81], a metric previously shown to strongly correlate with *in situ* pressures is plotted against peak ARFI displacement amplitude that was measured using a push MI of 2.3 (Figure 3.13c), a metric which is directly correlated to energy deposition *in vivo* and is used as a proxy for peak *in situ* pressure

herein. A linear regression found the peak ARFI displacement to moderately correlate with HSC with $r^2 = 0.47$.

3.4 Discussion

SWS yield increased while increasing push MI through body walls, which, as expected resulted in higher shear wave displacement amplitudes. In Figure 3.9b, median displacement amplitude was shown to increase with increasing push MI through body walls. Figure 3.9a also confirmed that median displacement amplitudes for successful SWS estimates were significantly higher than median displacement amplitudes for failed SWS estimates. Thus, in Figure 3.3, both DAX and L7-4 tracked SWSs demonstrate monotonically increasing SWS yield as a function of increasing push MI.

Motion estimation jitter magnitude also contributes to SWS yield, which is demonstrated when comparing tracking through body wall and without body wall (imaging combination 1 to 2). Without the body wall, the average jitter magnitudes across the track receive lines were equivalent between the DAX and L7-4, as shown in Figure 3.10, while jitter magnitudes increased considerably when tracking through body walls as seen in Figure 3.11. Furthermore, Figure 3.11 depicted the L7-4, without body wall presence, capable of tracking particle velocities of about 1/5 the magnitude of particle velocities visualized by the DAX through the body wall. Therefore, we conclude that tracking without body walls improved SWS yield via jitter reduction.

We also conclude from the data presented that while the presence of a body wall affected both the ability to push and track, the effects on tracking were more substantial. When using imaging combination 2 instead of 1 (i.e., to track without body walls compared to through body walls), SWS yield increased an average of 37% (Figure 3.3). When using imaging combination 3 instead of 1 to push without body walls, however, SWS yield only increased an average of 9% (Figure 3.6). Specifically, when matching the push and track MI across the SWEI tracking and ARFI pushing data (right most bars in Figures 3.3 and 3.6), SWS yield decreased from 85% to 46% with the addition of body walls on track (imaging combination 2 to 1) and SWS yield decreased from 53% to 47% with the addition of body walls on push (imaging combination 3 to 1). That was despite the presence of the body wall decreasing the median ARFI displacement from 2.33 μm to 0.43 μm in Figure 3.9b, which was a factor of 5.4 and similar to decreases shown in previous studies [28, 75]. This change in displacement amplitude was on the same order of magnitude as the jitter amplitude increase of 4.8 with body wall presence (Figure 3.11). Thus, the displacement to jitter ratio had not drastically changed. Two potential sources for the discrepancy in SWS yield between imaging combination 2 (push through and track without body wall) and 3 (push without but track through body walls) are reverberation clutter and phase aberration. Reverberation clutter has been shown to be generated in the body wall. In addition to decreasing pressure amplitude and thus

signal at the focus, reverberation clutter can write into the tracking data as multiplicative noise. This could lead to underestimation or even masking of particle motion.

The linear correlation between HSC and peak displacement shown in Figure 3.13 was moderate and lower than the strong correlation between HSC and *in situ* peak pressure as previously reported, likely due to differences in pulse duration. HSC was computed using a B-mode pulse while displacement was generated using a long, narrowband pulse. As such, phase aberrations of more than one wavelength could still sum coherently to generate energy for displacement for a push pulse while the same phase shifts would not contribute to the spatial coherence value we computed for our single-cycle coherence measurements.

Further increases in track MIs may have benefited SWS measurements through a few of the body walls. This is observed in Figure 3.13a which illustrated at least 4 body walls that had not reached harmonic LOC plateau by MI of 2.3. Since LOC plateau correlates with achieving optimal electronic SNR for B-mode imaging [62], we can postulate that SWEI electronic SNR was suboptimal and SWS measurements for those body walls could benefit if higher track transmit MI were permitted by the scanner software.

3.5 Conclusions

This study evaluated and quantified the impact of imaging through body walls on both ARFI push and MTL-SWEI track beams, and demonstrated that the effects on

the two were not equivalent. Body walls degrade MTL-SWEI tracking more severely than they degrade ARFI push pulses in terms of the resulting shear wave speed estimates. For MTL-SWEI tracking beams, the presence of body walls decreased SWS yield by an average of 37% across the 5 push MIs tested. For SWEI pushing beams, the presence of body walls decreased SWS yield by only an average of 9% across the 10 track MIs tested. These findings inform the focus of future sequence optimization in SWE imaging.

3.6 Conflict of Interest

Kathryn R. Nightingale has intellectual property related to radiation force-based imaging technologies that has been licensed to Siemens, Samsung and MicroElastic Ultrasound Systems.

3.7 Acknowledgements

This work was supported by NIH Grant R01 EB022106. The authors would like to thank Siemens Healthcare USA, Ultrasound Division for their in-kind technical support.

4 Quantifying the Impact of Abdominal Body Wall on *in situ* Peak Rarefaction Pressure during Diagnostic Ultrasound Imaging

This chapter has been published in the Ultrasound in Medicine & Biology journal under the same title. The contents of the journal publication are included in its entirety with formatting changed to be consistent with the rest of the dissertation. It was coauthored with Gianmarco F. Pinton, Yufeng Deng, and Kathryn R. Nightingale.

4.1 Introduction

Ultrasound is widely used for abdominal imaging and is the standard-of-care for hepatocellular carcinoma (HCC) screening [12, 13]. HCC screening with diagnostic ultrasound imaging results in successful diagnosis for only 25-60% of patients [14-17]. The high failure rate of HCC diagnosis with ultrasound is attributed to poor image quality. Poor image quality is common even though Tissue Harmonic Imaging (THI) [21], the current standard mode for hepatic imaging, produces higher quality images than traditional fundamental frequency imaging [8, 22-24]. One reason for poor image quality is that, due to its harmonic nature, THI has a lower signal-to-noise ratio (SNR) as compared to fundamental signals [9]. Low SNR is associated with lower B-mode contrast and CNR and increased displacement estimation jitter [51, 85]. We have observed moderate B-mode and considerable ARFI/SWE improvements in performance when imaging with $MI > 1.9$ [27, 28]. We have also demonstrated a linear correlation between harmonic image quality and increasing transmit pressures until a maximum

plateau is observed [62], but the transmit pressure associated with this maximum varies considerably between patients [62]. We hypothesize that these differences are associated with differences in *in situ* signal levels, which has motivated the work herein.

Diagnostic ultrasound transmit pressures are assessed by the FDA guideline for Mechanical Index (MI) through Equation 4.1 (also Equation 2.4 in Chapter 2), with a guideline for a maximum value, and thus a *de facto* upper limit of 1.9 [25].

$$MI = \frac{p_{r0.3}(Z_{MI})}{\sqrt{f_{awf}}} \quad (4.1)$$

In Equation 4.1, $p_{r0.3}(Z_{MI})$ is the estimated *in situ* peak rarefaction pressure (PRP) amplitude. f_{awf} is the acoustic working frequency of the pressure waveform. $p_{r0.3}(Z_{MI})$ is determined from PRP measured in water, $p_r(Z_{MI})$, and linearly derated by $\alpha = 0.3\text{dB/cm/MHz}$ as seen in Equation 4.2.

$$p_{r0.3}(Z_{MI}) = p_r(Z_{MI})e^{-\alpha*Z_{MI}*f_{awf}} \quad (4.2)$$

The MI equation is a first order approximation model that is simple and easy to use. However, there are some limitations associated with the assumptions in this model. Ultrasound propagates differently in water as compared to tissue. At medical diagnostic frequencies of a few megahertz, water is minimally attenuating and exhibits a frequency squared dependence at $0.00139\text{dB/cm/MHz}^2$ [86] compared to the typical soft tissue range of 0.3-1.1 dB/cm/MHz [77-79] which allows shocks to form more quickly in water. The formation of shocks in water causes more energy to be lost due to saturation [87]. In addition, tissue has heterogeneity in its material properties that is not accurately

modeled by the constant attenuation value employed by the MI. Due to these factors, *in situ* PRP can often be overestimated and/or underestimated by the MI calculation.

The work presented herein includes numerical simulations along with *in situ* experimental validation. The simulations explore the factors that cause the MI to inaccurately estimate PRP *in situ* and assess the range of *in situ* values that can occur *in vivo*. *In situ* experimental results confirm the simulation validity. Throughout this work, we report an effective Mechanical Index (MIE) by employing the actual simulated or measured *in situ* PRP in the numerator of Equation 4.1 instead of that determined by linearly derating water-based measurements [54].

4.2 Methods

4.2.1 Simulations

Because analytical solutions to the nonlinear wave equation in heterogeneous media were not available, we chose to numerically model wave propagation with a second order nonlinear full-wave equation that describes nonlinear wave propagation through an attenuating media [88]. The simulations allowed us to analyze the effects of different abdominal wall models on PRP and to accurately control material properties.

The simulation source pressures corresponded to experimentally measured source pressures from a typical abdominal harmonic imaging sequence using a 4C1 curvilinear transducer on a Siemens Acuson S3000 scanner (Siemens Healthcare, Issaquah WA USA) with the following transmit parameters: an F/1.5 transmit, 2-cycle

excitation, at a center frequency of 2.2 MHz, focused at 5 cm axially. The transmit pressures corresponded with an MI of 1.9 measured at the focus. Pressure signals were measured using an Acertara 804 PVDF membrane hydrophone (Acertara Acoustic Laboratories, Longmont CO USA) and recorded using a LeCroy Wavesurfer MXs-B oscilloscope (Teledyne LeCroy, Chestnut Ridge NY USA). The membrane hydrophone had magnitude calibration from 1-20 MHz and a spot size of 0.6 mm, sufficient for the low 2.2 MHz center frequency [84]. Consistent with all of our experimental measurements presented, frequency deconvolution was applied to the voltage signal data to derive the pressure waveforms [83]. Source pressures were collected in a plane perpendicular to the propagation direction at a distance of 2 mm from the face of the transducer. Secured to a computer controlled 3-axis translation stage (Newport Corporation, Irvine CA USA) with 10 μm precision, the transducer was moved laterally and elevationally in increments of 0.175 mm to collect the data plane. These pressures were then numerically back-propagated using the full-wave model to the curved surface of the transducer aperture. This allowed for accurate source pressure characterization from the curved surface to be forward propagated through media with varying properties.

Acoustic propagation through various materials was simulated using the full-wave method in 3D [89]. This nonlinear simulation package was chosen because it captures multiple reflections and path heterogeneity. For this finite-difference time-

domain method, we used a regularly sampled Cartesian grid for the simulations with a spacing of $44\ \mu\text{m}$ to guarantee accuracy up to the second harmonic.

In order to accurately simulate path heterogeneity, image data from the Visible Human abdominal region [90] was used to derive acoustic property maps for propagation (Figure 4.1a). The image stack was first cropped for the abdominal region. Then, layers of skin, fat, muscle, and liver were segmented using a threshold-based algorithm [89]. Tissues within each layer were categorized into connective tissue, fat, muscle, and liver using a combination of histogram equalization, edge detection, and morphological operations (Figure 4.1b). Because skin and connective tissue have similar acoustic properties, they were both categorized as connective tissue. The four tissue maps were then converted to attenuation, nonlinearity, speed of sound, and density maps for each simulation (Table 4.1). A total of five non-overlapping abdominal sections were used to generate five different body wall simulations. Each simulation took 120 hours to run using a 48-computer server cluster running at 2.6 GHz clock speed and using 120 GB of RAM.

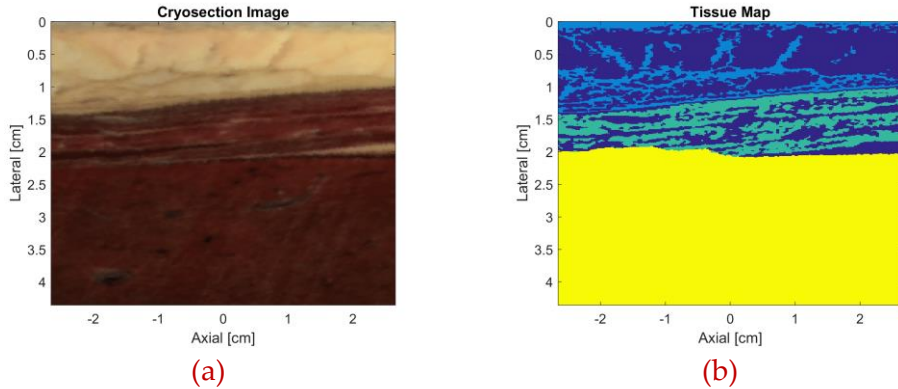


Figure 4.1: Sample image slice of abdominal wall from the Visible Human cadaver (a). Resulting tissue type map (b) after segmentation, thresholding, and feature detection. Dark blue: fat. Light blue: connective tissue. Green: muscle. Yellow: liver.

Table 4.1: Simulated Tissue Acoustic Properties referencing [77-79]. Iso-Velocity columns determined by shifting speed of sound differences into density differences. Iso-Impedance columns determined by changing density to maintain consistent impedance.

Tissue Type	α (dB/cm/MHz)	B/A	ρ (kg/cm ³)	c (m/s)
Connective	0.5	8	1120	1613
Fat	0.4	9.6	937	1479
Muscle	1.15	9	1070	1566
Liver	0.5	7.6	1064	1570
Phantom	0.5	10	1000	1540
Tissue Type	Iso-V ρ (kg/cm ³)	Iso-V c (m/s)	Iso-Z ρ (kg/cm ³)	Iso-Z c (m/s)
Connective	1173	1540	1120	1613
Fat	900	1540	1222	1479
Muscle	1088	1540	1154	1566
Liver	1085	1540	1151	1570

4.2.2 *In situ* Experiments

The experimental setup shown in Figure 4.2 was used to measure *in situ* PRP through porcine abdominal body wall samples at room temperature (22 °C). The samples were degassed prior to the experiments to remove air pockets. We secured 2-3

cm thick fresh pork belly samples from the local grocery market to the face of a curvilinear Siemens 4C1 transducer by compressing the body walls into the transducer face with two supports shown in Figure 4.2. The pork belly included the skin, fat, and muscle layers. In order to facilitate the scanning motion involved for hydrophone measurements, an attenuating fluid, comprised of evaporated milk, deionized water, and salt, (tuned to $\alpha = 0.5$ dB/cm/MHz and sound speed of 1540 m/s) was used to model liver tissue [79]. The transducer transmit configuration was matched to the simulations with a 2-cycle excitation with a center frequency of 2.2MHz, and a F/1.5 focal configuration with a focus at 5cm axially. *In situ* pressures were measured as described above. The transducer and each abdominal slab were mounted to a computer-controlled Newport 3-axis translation stage to measure pressures throughout a $1.5 \times 3 \times 30$ mm ROI around the focus with $0.1 \times 0.2 \times 1$ mm spacing. *In situ* pressure fields were compared with linearly derated PRP in water.

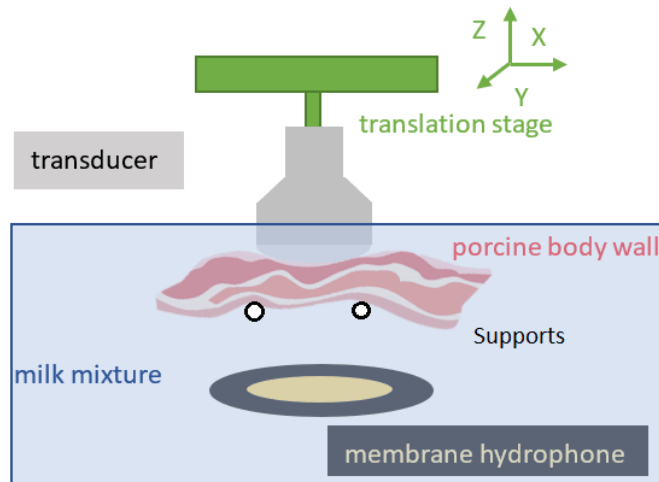


Figure 4.2: Experimental setup for scanning *in situ* PRP field with the membrane hydrophone. Transducer was mounted to the translation stage. The pork belly was secured to the transducer face using two support fixtures. The PVDF membrane hydrophone was in a fixed position submerged in the evaporated milk mixture.

4.3 Results

4.3.1 Simulation Validation

We compared experimentally measured peak negative pressures from propagation through an attenuating fluid with a measured attenuation of $\alpha = 0.5$ dB/cm/MHz, sound speed of 1540 m/s and filtered the waveforms with a range of cutoff frequencies to assess the impact of including different harmonics as shown in Figure 4.3a. Also shown in Figure 4.3b is the PRP of the waveform as a function of the number of harmonics included.

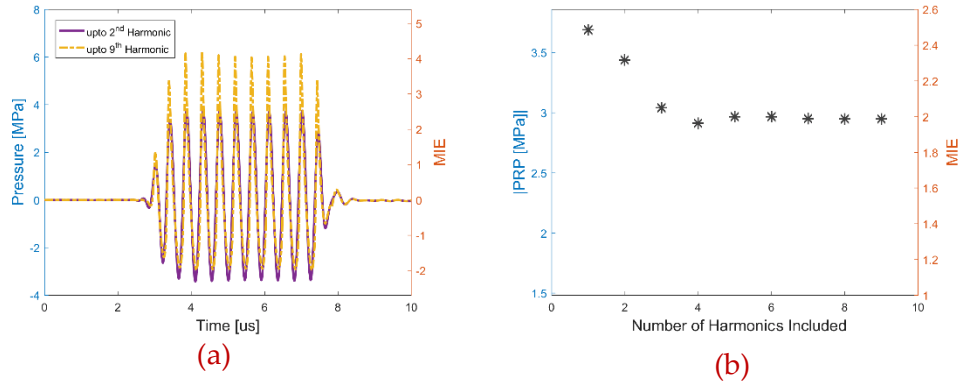


Figure 4.3: Experimentally measured MIE pressure waveforms from propagation through milk mixture with an attenuation coefficient of $\alpha = 0.5$ dB/cm/MHz. We filtered the signal to remove higher order harmonics with different cutoff frequencies for better comparison with the simulation results. (a) shows the waveform with 2 and 9 harmonics, (b) shows the PRP as a function of the number of harmonics included after filtering with various cutoff frequencies.

4.3.1.1 Material Nonlinearity Parameter

We simulated propagation through homogeneous media while varying the nonlinearity parameter from $B/A = 5$ to 10 based on the range for normal soft tissue [78, 91]. Attenuation was fixed to $\alpha = 0.3$ dB/cm/MHz and the full F/1.5 aperture was used. Figure 4.4a demonstrates that the resulting PRP magnitude and MIE remained consistent to within 1% across the entire range of B/A studied. Additionally, Figure 4.4b shows that the PRP axial position also remained unchanged to within one wavelength (0.7 mm) of the 5.0 cm focus across the entire range of B/A simulated.

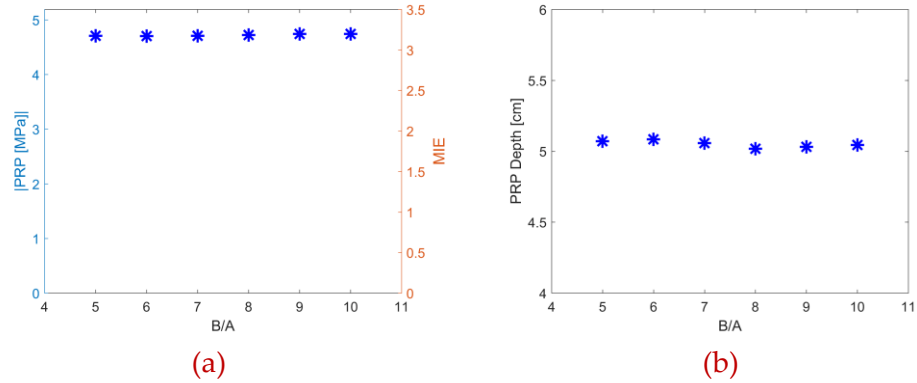


Figure 4.4: Simulated PRP magnitude and MIE (a) as a function of nonlinearity parameter (B/A). (b) Axial position of PRP as a function of the same range of B/A.

4.3.1.2 Material Attenuation

The effects of changing attenuation were simulated in homogeneous media using a fixed B/A of 10 and the full F/1.5 aperture. Attenuation was varied from $\alpha = 0.3$ to 1.1 dB/cm/MHz. Figure 4.5a shows that *in situ* PRP magnitude and corresponding MIE decreases across the attenuation range tested. Figure 4.5b shows that throughout the entire range of attenuation simulated, the PRP does not shift spatially more than a single wavelength (0.7mm) axially from the 5.0 cm focus.

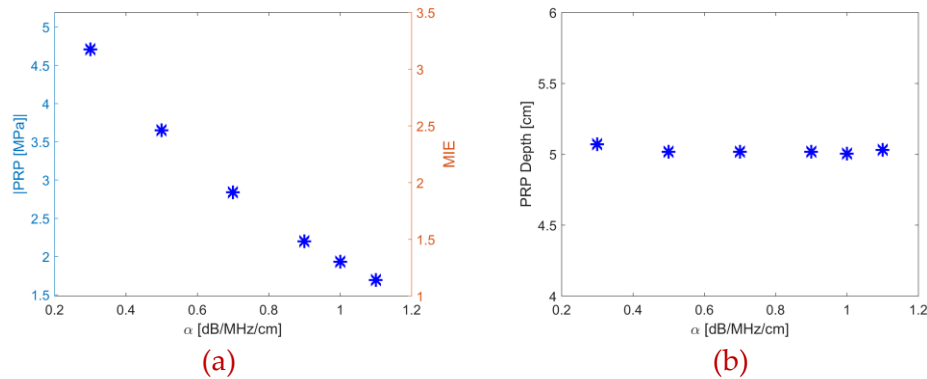


Figure 4.5: Simulated PRP magnitude and MIE (a) as a function of material attenuation (α). (b) Axial position of PRP as a function of the same range of attenuation.

4.3.1.3 Medium Aperture (F/3) Path Heterogeneity

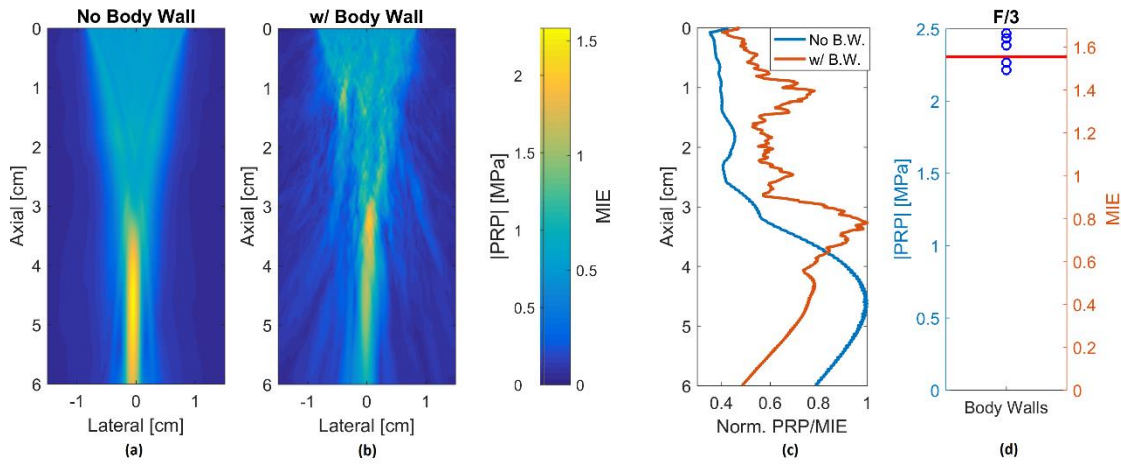


Figure 4.6: Simulated lateral-axial *in situ* PRP/MIE beam plot along the center elevation slice for an F/3 transmit (a) focused at 5cm axially after propagation through homogeneous $\alpha = 0.5$ dB/cm/MHz material. (b) The same *in situ* PRP/MIE beam plot as result of propagation through a heterogeneous body wall map and liver with the same color bar as (a). (c) Axial distribution of normalized PRP/MIE for the F/3 transmit when propagated through homogeneous $\alpha = 0.5$ dB/cm/MHz material (blue), and when propagated through a heterogeneous body wall map and liver (red). (d) *in situ* PRP/MIE from 5 different heterogeneous body wall maps (blue circles) compared against *in situ* PRP/MIE through homogeneous $\alpha = 0.5$ dB/cm/MHz material (red horizontal line).

We simulated an F/3 transmit aperture, a typical clinical B-mode imaging aperture, through homogeneous material and heterogeneous body wall maps. Example spatial distributions of *in situ* PRP/MIE in the lateral-axial center plane for propagation through homogeneous $\alpha = 0.5$ dB/cm/MHz material and a heterogeneous body wall map are shown in Figure 4.6a, b. Although the two plots show different beam profiles, they retain similar *in situ* PRP/MIE as noted by the color bar.

Figure 4.6c illustrates the axial profiles of the normalized PRP for the two simulations shown in Figure 4.6a, b. The PRP peaked at a depth of 4.6 cm for the

homogeneous material compared to a depth of 3.3 cm for the sample body wall map.

For all 5 body wall maps, the depth of the PRP was consistently shallow to the homogeneous case ranging 1-1.5 cm closer to the transducer face.

Figure 4.6d compares the *in situ* PRP/MIE through the 5 body wall maps for the F/3 transmit against that predicted by propagation through homogeneous $\alpha = 0.5$ dB/cm/MHz material. The body wall maps yielded *in situ* PRP/MIE (2.2-2.5 MPa/1.5-1.7 MIE) similar to that through the homogeneous case (2.3 MPa/1.6 MIE). The *in situ* PRP/MIE estimates predicted by the homogeneous material resulted in error within 8% for this focal configuration.

4.3.1.4 Large Aperture (F/1.5) Path Heterogeneity

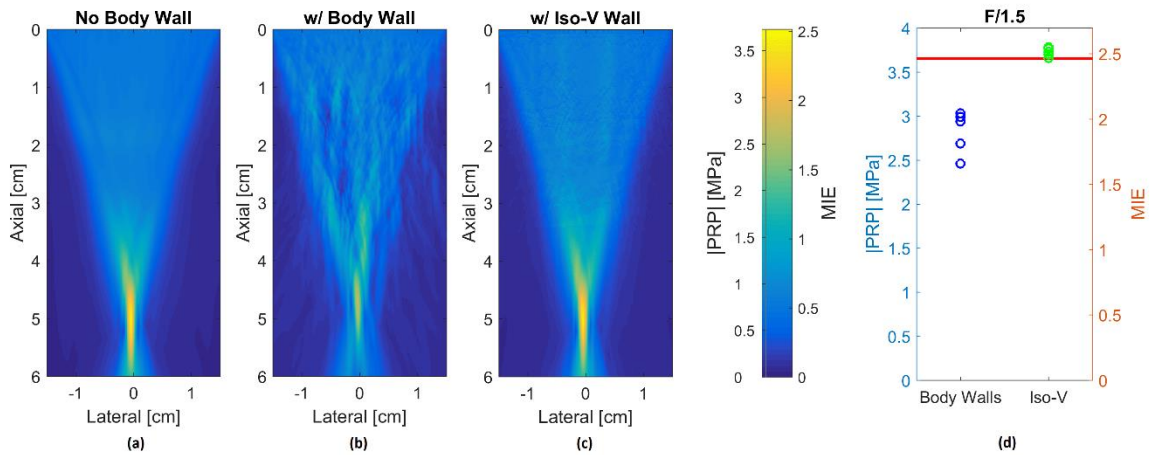


Figure 4.7: Simulated *in situ* PRP/MIE spatial distributions of an F/1.5 transmit in lateral-axial view from propagation through (a) homogeneous $\alpha = 0.5$ dB/cm/MHz material, (b) a body wall map, and (c) the same body wall map with iso-velocity modification. (d) Comparison of *in situ* PRP/MIE predicted for an F/1.5 transmit condition using homogeneous propagation material (horizontal red line) with 5 body wall maps (blue circles), and 5 iso-velocity (Iso-V) modified body walls (green circles).

Next, we simulated an F/1.5 transmit aperture, often used for ARFI and SWEI pushing [28, 41] and STL-SWEI tracking beams [27], through homogeneous material and heterogeneous body wall maps. Figure 4.7a, b shows sample *in situ* PRP/MIE lateral-axial beam plots in the center elevation plane for the F/1.5 transmit aperture configuration. Comparing the body wall case from Figure 4.7b to the homogeneous $\alpha = 0.5$ dB/cm/MHz case in Figure 4.7a, there is a 26% decrease in PRP magnitude/MIE. Figure 4.7d illustrates the same trend seen in Figure 4.7b. Propagation through each of the 5 body walls resulted in smaller *in situ* PRP magnitudes and MIE (2.46-3.03 MPa/1.66-2.04 MIE) than the homogeneous case (3.65 MPa/2.46 MIE). For all 5 body wall maps, the depth of the PRP ranged between 3.8 and 4.7 cm.

Tissue heterogeneity is known to cause local sound speed differences [92]. Sound speed differences lead to phase aberration which distorts the focus. To isolate and remove the effects of phase aberration, we ran simulations setting sound speeds of all four tissue types to 1540 m/s while maintaining the original acoustic impedance of each tissue by modulating density values (Table 4.1), thus creating iso-velocity simulations. Figure 4.7c shows a lateral-axial *in situ* PRP/MIE beam plot through the center elevation slice from the iso-velocity body wall map. The beam plot shape and PRP magnitude/MIE in Figure 4.7c are more concordant with Figure 4.7a than Figure 4.7b. In fact, PRP magnitude/MIE for the sample iso-velocity body wall differed from the homogeneous case by less than 4%. Furthermore, Figure 4.7d demonstrates that all 5

body wall samples with the iso-velocity implementation exhibit *in situ* PRP/MIE within 5% of the homogeneous $\alpha = 0.5\text{dB/cm/MHz}$ case.

4.3.1.5 Small Aperture (F/5) Path Heterogeneity

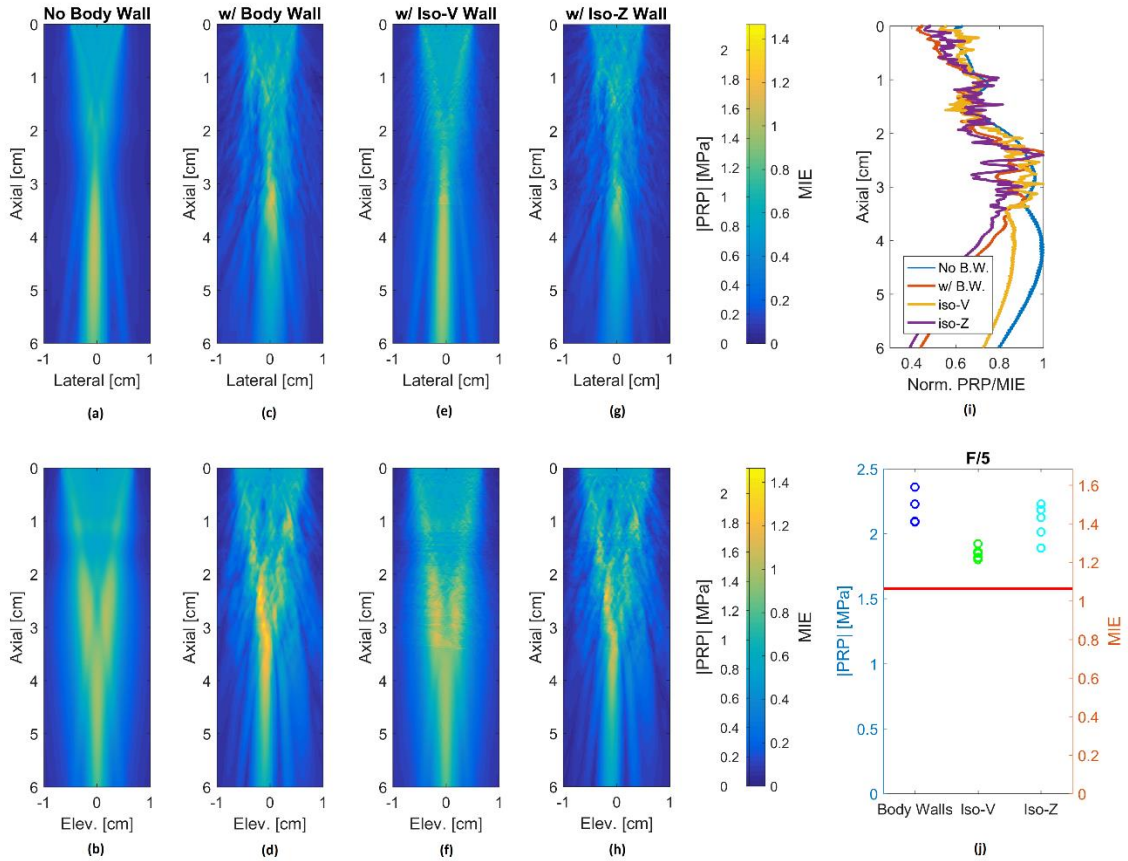


Figure 4.8: Simulated *in situ* PRP/MIE spatial distributions of an F/5 transmit in lateral-axial and elevation-axial planes from propagation through (a)(b) homogeneous $\alpha = 0.5 \text{ dB/cm/MHz}$ material, (c)(d) a body wall map, (e)(f) the same body wall map with iso-velocity modification, and (g)(h) the same body wall map with iso-impedance modification. (i) Axial distribution of normalized PRP/MIE for the F/5 transmit when propagated through homogeneous $\alpha = 0.5 \text{ dB/cm/MHz}$ material(blue), when propagated through a heterogeneous body wall map and liver(red), when propagated through the body wall with iso-velocity modification (orange), and when propagated through the body wall with iso-impedance

modification (orange). (j) Comparison of *in situ* PRP/MIE predicted for an F/5 transmit condition using homogeneous propagation material (horizontal red line) with regular body walls (blue), iso-velocity (Iso-V) body walls (green), and iso-impedance (Iso-Z) body walls (cyan).

A small transmit aperture (F/5), as might be employed when performing intercostal imaging [93], imaging larger patients [94], or synthetic aperture imaging [95], was analyzed. Figure 4.8a, b illustrates the PRP/MIE beam plots for the center lateral-axial and elevation-axial planes of the $\alpha = 0.5$ dB/cm/MHz homogeneous media simulation. Figure 4.8c, d depict the same beam plot planes for the sample body wall case. Plotted on the same PRP/MIE axis, the beam plots for the body wall case demonstrate an increase in PRP/MIE of 40% over the homogeneous case. Figure 4.8j confirms that each of the 5 body walls consistently cause higher *in situ* PRP/MIE (2.1-2.4 MPa/1.4-1.6 MIE) compared to the homogeneous case (1.6 MPa/1.1 MIE). Figure 4.8i depicts the axial profiles of the normalized PRP for the simulations. While the normalized PRP peaked at 4.2 cm depth for the homogeneous case, the peak occurred at 2.4 cm in depth for this sample body wall; this position was in the body wall.

Similar to the large aperture F/1.5 case, the iso-velocity modification was made for the F/5 configuration to remove phase aberration. Figure 4.8e, f present the beam plots for the sample body wall with iso-velocity modifications. The beam plots restore the general shapes seen for the homogeneous case (Figure 4.8a, b) and decrease in magnitude from the un-modified body wall case. Figure 4.8j plots the *in situ* PRP/MIE

for the 5 iso-velocity modified body walls (1.80-1.92/1.21-1.29 MIE). The 3.0 cm PRP depth also shifted closer to the transducer focal depth (Figure 4.8i).

For further analysis, acoustic impedance mismatches in tissue were isolated by maintaining the original tissue speed of sound and modifying the density values such that the acoustic impedance (sound speed x density) was constant (Table 4.1). Figure 4.8g, h illustrate the beam plots for the sample body wall with iso-impedance modification. For the iso-impedance body wall, PRP amplitude decreased from the original body wall while retaining a similar beam plot shape. The range of *in situ* PRP/MIE for the 5 iso-impedance modified body walls (1.89-2.23 MPa/1.27-1.50 MIE) as depicted in Figure 4.8j is still above the homogeneous case by 20-41%. The PRP depth for the iso-impedance modified sample body wall shifted to 2.4 cm (Figure 4.8i).

4.3.2 Experimental Results

In order to validate the simulation results, we evaluated the F/1.5 focal configuration experimentally by scanning through porcine body walls submerged in $\alpha = 0.5$ dB/cm/MHz milk solution. The milk solution sound speed, density, and acoustic attenuation made it a suitable liquid liver phantom and coupling medium. Figure 4.9a shows a sample spatial peak intensity waveform obtained through a 2.4 cm body wall in the liquid liver phantom and the corresponding linearly derated water waveform. The time difference between the two waveforms arises from differences in sound speed for the two configurations and the shallow PRP location through the body wall. The plot

depicts *in situ* PRP/MIE through the body wall to be more than 50% lower in magnitude than the linearly derated PRP (1.39 vs 2.82 MPa and 0.94 MIE vs 1.9 MIE, respectively). Figure 4.9b shows the waveforms in the frequency domain to illustrate the effects of both nonlinear propagation and attenuation through the body wall; higher harmonics were preferentially attenuated in the tissue as compared to the water with fewer harmonics present. For the waveform in water, the second harmonic was -9 dB from the fundamental whereas the second harmonic was -19 dB from the fundamental signal for the measurement through tissue and milk.

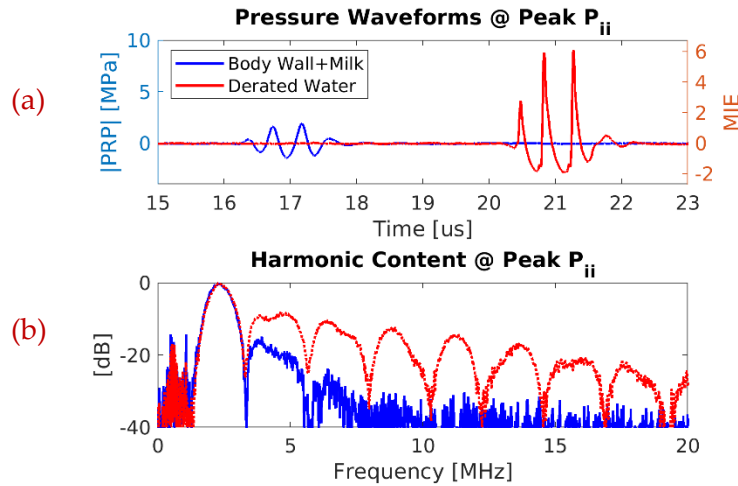


Figure 4.9: Peak intensity pressure waveform (a) from propagation through a body wall sample and $\alpha = 0.5$ dB/cm/MHz milk solution (blue) and derated peak intensity pressure waveform from propagation through DI water (red). (b) The same waveforms shown in the frequency domain.

The normalized intensity profiles for the beamforms in Figure 4.9 are plotted in the lateral/elevational plane for Figure 4.10. The body wall + attenuating fluid case has a 43% wider lateral FWHM compared to purely water case.

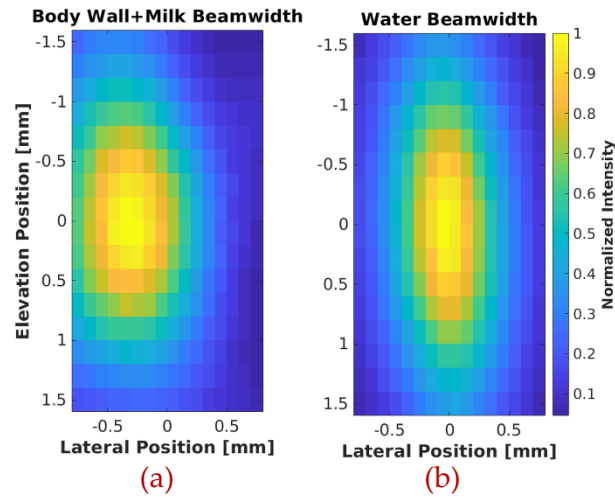


Figure 4.10: Lateral-elevation transmit intensity beamwidth at PRP depth (a) when propagated through a body wall sample. Lateral-elevation transmit intensity beamwidth at PRP depth (b) when propagated through water.

Similar to the sample body wall in Figure 4.9, all 9 body walls caused *in situ* PRP/MIE to be consistently lower in magnitude compared to the derated water MI prediction, ranging between 15-82% of the MI prediction (Figure 4.11). There was no correlation between body wall thickness and *in situ* PRP/MIE in these data ($r^2 = 0.074$).

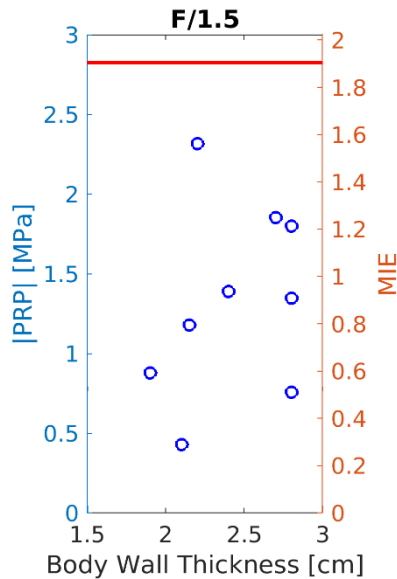


Figure 4.11: *In situ* PRP/MIE measured through 9 body walls compared to that estimated by the MI (Horizontal red line represents the FDA guideline of 1.9) as a function of the body wall thickness. Linear regression indicates that these parameters are uncorrelated ($r^2 = 0.074$).

4.4 Discussion

The simulation results (Figure 4.3) were validated by matching the experimental results (Figure 4.5) in $\alpha = 0.5$ dB/cm/MHz material to within 5% with MIEs of 2.45 and 2.35, respectively.

From the simulated parametric analysis through a homogeneous material, we found that neither nonlinearity nor attenuation led to large translations of the PRP's axial spatial location (< 0.7 mm) (Figures 4.4b, 4.5b). This is because the PRP spatial location in a homogeneous medium was determined by the geometric focus and center frequency of the pulse. Additionally, changing nonlinearity within the range reported for tissue did not change the PRP magnitude/MIE by more than 1% (Figure 4.4a). As

expected, increasing material attenuation decreased the PRP magnitude/MIE because more energy was lost before reaching the focus (Figure 4.5a).

When simulating propagation through heterogeneous body walls for the F/3 transmit configuration, linearly derated MI predicted *in situ* PRP/MIE for the 5 simulated body walls to within $\pm 8\%$ error (Figure 4.6d). Given that hydrophone calibrations are accurate to within ± 1 dB for the frequency range of interest [96-98], we conclude that MI accurately estimated *in situ* PRP/MIE for all 5 body walls for the F/3 transmit configuration.

When simulating the more tightly focused F/1.5 transmit configuration, the linearly derated MI consistently overestimated *in situ* PRP/MIE for the 5 simulated body walls by 20-48%. The experimental measurements using the matched F/1.5 focal configuration corroborated the simulation findings. The linearly derated water measurement consistently overestimated *in situ* PRP/MIE in all 9 pork belly slabs (Figure 4.11). *In situ* PRP/MIE measured through the body walls ranged between 15-82% of the linearly derated MI prediction, encompassing the range seen in simulation, thus confirming that the linearly derated MI overestimates *in situ* PRP/MIE for a large F/1.5 transmit configuration.

One possible reason for the overestimation by MI is the distorted beam patterns that were consistently observed at the focus. Broadened transmitted beamwidth was observed in the lateral and elevation dimensions (Figure 4.10). The transmitted

beamwidth was shown to broaden by more than 40% when propagated through the body wall compared to in water. Beamwidth broadening is associated with phase aberration [24, 99]. Phase aberration refers to local speed of sound differences across the transmit aperture. These local sound speed offsets caused the wavefronts to arrive at the focus at different times, thus not coherently summing at the focus which resulted in decreased pressure amplitudes at the focus. To eliminate the effects of phase aberration in our simulations, we created the iso-velocity modification while maintaining the acoustic impedance difference between tissue types by modulating the density (Table 4.1). For the F/1.5 transmit, the iso-velocity modified body walls reduced the difference between *in situ* PRP/MIE and linearly derated MI to < 5%. In fact, the elimination of phase aberration introduced slight underestimation by < 5% which likely occurred due to the slightly lower mean attenuation of the body walls compared to the homogeneous case (0.46 vs. 0.5 dB/cm/MHz). Because the iso-velocity body wall maps eliminated the overestimation of PRP by MI, we conclude that phase aberration is the primary source of the overestimation of MI by linear derating for tightly focused transmits.

When simulating the weakly focused F/5 transmit configuration, MI consistently underestimated *in situ* PRP/MIE for the 5 simulated body walls by 32-50%. When phase aberration was removed by using iso-velocity modified body wall maps, the MI underestimation reduced to 14-22%. Although the results suggested that phase aberration contributes to the inaccuracy of MI for the F/5 transmit, it is not the only

important factor. In addition to phase aberration, tissue heterogeneity also introduced reverberation. Reverberation is the multiple reflections caused by impedance differences between tissue types. When phase aberration was removed by using iso-impedance modified body wall maps, the MI underestimation ranged 20-41%. Unlike the removal of phase aberration, where the beam profile was similar to the no body wall case, iso-impedance body walls did not restore the beam focus (Figure 4.8). Rather, with less energy lost to reflections, the constructive interference caused by phase aberration was more pronounced. Both phase aberration and reverberation caused *in situ* PRP/MIE to be inaccurately estimated by MI for the F/5 transmit.

For this weakly focused F/5 transmit configuration, the acoustic impedance difference at the internal tissue boundaries, local speed of sound differences, and attenuation all competed against the focal gain. First, due to the large F/ number, focal gain was weak. Then, the peak pressure at the focus was decreased by phase aberration as in the large aperture case. At the same time, tissue boundaries with sound speed and impedance differences cause beam distortion and constructive interference at depths shallow to the transducer's geometric focus. At these shallower depths, the ultrasound beams have propagated shorter distances, therefore experiencing less attenuation. These factors work in concert to cause larger peak pressures in the nearfield than at the focal depth for the weakly focused case. These phenomena are observed in Figure 4.8b, e

where the PRP axial position shifted from the 4.3 cm depth to 2.4 cm from the transducer face where it was still in the body wall.

Like the F/5 scenario where PRP was drawn closer to the transducer face, the F/3 simulations also experienced this (Figure 4.6). For this transmit, however, focal gain was sufficiently strong such that the PRP remained closer to the focus at 3.3-4.0 cm depth. At these depths, the focal gain balanced against sound speed differences, impedance differences and attenuation to maintain the PRP/MIE predicted by MI.

The results from the different transmit aperture sizes offer insight to the feasibility of using elevated acoustic output safely in the clinical setting. MI estimation of *in situ* PRP/MIE is most inaccurate at large and small apertures. The underestimation at small apertures should not impact the use of elevated acoustic output as small apertures are generally not able to generate $MI > 1.9$. However, large apertures are often used in ARFI and SWEI imaging for both pushing and sometimes tracking. Clinical ARFI and SWEI studies have routinely reported measurement failure at imaging depths greater than 7 cm, and in patients with high BMI and in stiffer livers [100, 101]. Studies using large aperture transmits have demonstrated significant improvement in SWEI measurement success for human subjects when using SWEI push $MI > 1.9$ [28] and SWEI with focused track $MI > 1.9$ [27]. The consistent overestimation of *in situ* PRP/MIE for large apertures demonstrated herein suggests a clinical benefit to employing elevated acoustic output on a patient specific basis for SWEI imaging when measurement failures

occur. The consistent overestimation of *in situ* PRP/MIE for large apertures suggests that the use of elevated output ($MI > 1.9$) with these apertures could be employed while remaining within the spirit of the MI guidance.

4.5 Conclusions

This study demonstrated that the MI can both overestimate and underestimate *in situ* PRP/MIE by more than 50% when imaging through the body wall depending upon focal configuration. For a large aperture (F/1.5), phase aberration was found to be the dominant factor leading to MI overestimation of *in situ* PRP/MIE. For a medium aperture (F/3), MI was found to accurately estimate *in situ* PRP/MIE. For a small aperture (F/5), phase aberration and reverberation clutter both contributed to higher *in situ* PRP/MIE compared to the MI estimate. Normal variation of nonlinearity in tissue does not cause measurable changes in *in situ* PRP/MIE. In addition, we found that changes in B/A and attenuation do not significantly affect the position of PRP. For large apertures, like F/1.5, there is ample room to increase source pressures while maintaining $MIE < 1.9$ when imaging through distorting body walls. Developing a method to more accurately estimate *in situ* PRP would thus enable adaptive transmit pressures based upon *in situ* estimates, which could in turn improve diagnostic performance while staying within the spirit of the FDA safety guidelines.

4.6 Acknowledgements

This work was supported by NIH Grant R01 EB022106. The authors would like to thank Siemens Healthcare USA, Ultrasound Division for their in-kind technical support.

5 On the Relationship between Spatial Coherence and *in situ* Pressure for Abdominal Imaging

This chapter has been published by the Ultrasound in Medicine & Biology journal under the same title. The contents of the journal publication are included in its entirety with formatting changed to be consistent with the rest of the dissertation. It was coauthored with Gianmarco F. Pinton, and Kathryn R. Nightingale.

5.1 Introduction

Ultrasonic techniques, such as B-mode and elasticity imaging, are standards-of-care for many liver imaging scenarios including hepatocellular carcinoma (HCC) screening [12, 13] and chronic diffuse liver disease evaluation [102-104]. Tissue Harmonic Imaging (THI) [21], the current clinical standard for hepatic B-mode imaging, has been adopted because of its ability to generate higher quality images than traditional fundamental frequency imaging [8, 22-24]. Tissue harmonic signal has offered similar benefits for elasticity imaging [50], which has led to harmonic signal also being utilized for clinical shear wave elasticity imaging (SWEI) in the liver. Harmonic signals, however, are often 15-20 dB lower in amplitude than the corresponding fundamental signals and can approach the level of the electronic system noise [57]. When the harmonic signals are signal-to-noise ratio (SNR) limited during clinical imaging, diagnostic utility is decreased [18, 105, 106]. The logical solution for low SNR is to increase signal strength. Previous studies have shown improvements in clinical yield when using MIs exceeding the FDA guidelines for SWEI pushing and tracking

sequences [27, 28, 41] along with modest image quality improvements in THI B-mode imaging [107]. Ultrasound pressure amplitudes are indirectly limited by the FDA guideline for Mechanical Index (MI). The *de facto* limit arising from FDA guidelines for MI is a value of 1.9 [25]:

$$MI = \frac{p_{r0.3}(Z_{MI})}{\sqrt{f_{awf}}} \quad (5.1)$$

In Equation 5.1 (also Equation 2.4 in Chapter 2 and Equation 4.1 in Chapter 4), $p_{r0.3}(Z_{MI})$ is the estimated *in situ* peak rarefaction pressure (PRP) amplitude. f_{awf} is the acoustic working frequency of the pressure waveform. $p_{r0.3}(Z_{MI})$ is determined from PRP measured in water, $p_r(Z_{MI})$, and linearly derated by $\alpha = 0.3\text{dB/cm/MHz}$ as seen in Equation 5.2 (also Equation 4.2 in Chapter 4).

$$p_{r0.3}(Z_{MI}) = p_r(Z_{MI})e^{-\alpha*Z_{MI}*f_{awf}} \quad (5.2)$$

The MI uses linear derating to provide a first order approximation of *in situ* pressure, but this is often inaccurate for predicting *in situ* PRP. In our previous work, we have shown that linear derating consistently overestimates the PRP (and thus MI) *in situ* for large aperture abdominal imaging configurations (i.e., F/1.5), and often underestimates the PRP for small aperture imaging configurations (i.e., > F/3) in abdominal imaging scenarios. For large focused transmit apertures, we determined the overestimation to be caused by beam spreading and defocusing associated with phase aberration during propagation through the body wall *in vivo*. Currently, there are no experimental measurement techniques that estimate *in situ* PRP while accounting for

effects of body-wall-dependent phase aberration in real-time. However, if a method could be developed to estimate *in situ* PRP with consideration of phase aberration, higher transmit pressures could be safely utilized while staying within the spirit of the FDA guideline. Herein, we explore the relationship between spatial coherence and PRP to determine if coherence could inform the development of *in situ* PRP estimation algorithms.

The Van Cittert–Zernike (VCZ) theorem [58, 59], was first developed for optics, and was applied to pulse echo ultrasound by Mallart and Fink [60]. The VCZ theorem predicts that spatial coherence from a diffuse, randomly scattering medium can be represented as the scaled Fourier transform of the transmit intensity profile or, equivalently, the autocorrelation of the transmit aperture function. Practically, this can be estimated from the cross correlation between time-delayed channel signals as a function of channel spacing or lag [60]:

$$\hat{R}(m) = \frac{1}{N-m} \sum_{i=1}^{N-m} \frac{\sum_{n=n_1}^{n_2} s_i(n) s_{i+m}(n)}{\sqrt{\sum_{n=n_1}^{n_2} s_i^2(n) \sum_{n=n_1}^{n_2} s_{i+m}^2(n)}} \quad (5.3)$$

In Eq. 5.3, $\hat{R}(m)$ is the normalized spatial coherence between transducer elements m apart. N is the total number of elements in the aperture. $S_i(n)$ is the time-delayed signal received by the i th element at sample n . $(n_2 - n_1)$ is the correlation kernel size.

In the case where the transmit aperture is an unapodized rectangle and the speckle acts as a diffuse, randomly scattering medium, the resulting predicted spatial coherence function is an isosceles triangle function with a base twice the width of the

transmit aperture centered at lag 0. By convention, only the positive lags are computed [99, 108].

With increasing phase aberration, the correlation between channels decreases [99]. As such, we hypothesize that spatial coherence can be used as a surrogate metric for phase aberration for large aperture abdominal imaging scenarios and that spatial coherence will be directly related to *in situ* PRP. Herein, we explore this hypothesis by quantifying the correlation between *in situ* PRP and spatial coherence using both simulations and *ex vivo* experiments.

5.2 Methods

Table 5.1: Simulated and Experimental Transducer Transmit Configuration.

Parameter	Simulation	Experiment
Tx center frequency (MHz)	2.2	1.6
Focal depth (cm)	5	6
F/#	1.5	1.5
# of active elements	80	125
Tx pulse length (cycles)	2	
Tx bandwidth		60%
# of adjacent beams	20	10
Beam spacing	Beamwidth/4	1.5 x beamwidth

5.2.1 Simulations

To simulate a clinical system, we modeled the source pressures from a diagnostic imaging transducer using the pulse inversion transmit configuration described in Table 5.1 with source pressure waveforms corresponding to a focal MI of 1.9. The finite

differences time domain (FDTD) solution of the 2D nonlinear wave equation described by Pinton [89], which models nonlinearity, attenuation, thermoviscous diffusivity, and variations in density, was used to model wave propagation in a heterogeneous attenuating medium while accounting for multiple scattering, reflection, and refraction. The heterogeneity of the acoustic propagation field parameters was determined by mapping tissue composition from 6 histologically stained human body walls [92] and 5 segmented photographs of human body walls [90] to speed of sound, density, attenuation, and non-linearity (B/A) for different tissue types with values described in Table 5.2 [77-79]. *In situ* PRP was then determined by quantifying pressure traces through time at all field locations and identifying the maximum PRP. To simplify comparisons between different body wall configurations, the effective Mechanical Index (MIE) [54, 70, 109] is reported herein, computed by estimating the attenuation along the propagation path, rather than assuming $\alpha = 0.3$ dB/cm/MHz.

Table 5.2: Simulated Tissue Acoustic Properties referencing [77-79] including phantom which mimics MI results.

Tissue Type	α (dB/cm/MHz)	B/A	ρ (kg/cm ³)	c (m/s)
Connective	0.5	8	1120	1613
Fat	0.4	9.6	937	1479
Muscle	1.15	9	1070	1566
Liver	0.5	7.6	1064	1570
Phantom	0.5	10	1000	1540

Each simulation spanned 4 cm by 7 cm (lateral x axial). Due to the FDTD nature of our simulation a sampling of 10 points per wavelength (PPW) was required. Since

accuracy up to the second harmonic was needed, sampling at 35 μm in both dimensions was chosen. 2D simulations were employed instead of 3D simulations to decrease computational overhead. In order to simulate the transducer-received waveforms used to compute spatial coherence, the received signals across the transmit aperture were averaged across every 11 simulation grid points laterally to simulate the 0.385 mm lateral pitch of each receive element in our experimental setup. Scattering was modeled by point variations of sound speed with random spatial position and uniform random amplitude (defined by the difference in speed of sound from the surrounding medium). The mean variation in the speed of sound for the scatterers was 5%. 40 point-scatterers per fundamental resolution cell were introduced to the simulation space to ensure fully developed speckle up to the second harmonic signal. Before computing the spatial coherence of the simulated channel data, appropriate focal delays were applied across the channels assuming a sound speed of 1540 m/s. The fundamental signal was extracted by subtracting the two pulse inverted signals and applying a 5th order low-pass Butterworth filter with a 3.3 MHz cutoff frequency while the harmonic signal was computed by adding the pulse inversion pairs and applying a 5th order band-pass Butterworth filter with cutoff frequencies of 3.3 and 5.5 MHz. Spatial coherence was then computed for both the fundamental and harmonic signals using the spatial covariance approach described by *Hyun et. Al* [110] with a kernel size of 3 wavelengths. We

investigated both the fundamental short-lag spatial coherence (SLSC) [108] and harmonic short-lag spatial coherence (HSC) [81] as computed by:

$$R_{sl} = \sum_{m=1}^M \hat{R}(m) \quad (5.4)$$

In Equation 5.4, $\hat{R}(m)$ is the normalized spatial coherence value between pairs of elements m apart. M is the maximum lag between elements that are summed to compute the coherence metric. R_{sl} is the summed spatial coherence value. Prior work in SLSC and HSC imaging recommends maximum lags between 5 to 25% of the transmit aperture because *in vivo* data has a spatial coherence length that typically does not span the entire aperture [81, 108]. Herein, $M = 20$ (i.e., the first 25% of the transmitting aperture) was used.

In situ PRP is only affected by the transmitted wave's forward propagation, thus the wave-front is aberrated one-way through the body wall. Spatial coherence, however, is computed from the backscattered signals that have also been aberrated during the return trip to the transducer face. As such, we hypothesized that spatial coherence would better correlate with *in situ* PRP if phase aberration could be removed during the backscattering process, which of course could only be modeled in simulation. To test this hypothesis, an additional round-trip simulation was performed with aberration only during forward propagation by replacing the body wall with homogeneous (liver) material properties halfway through the round-trip simulation. Channel pressure data was then collected as in the previous simulations. The spatial coherence and SLSC were

then calculated for this round-trip simulation case which controlled for one-way aberration during propagation.

5.2.2 *In situ* Experiments

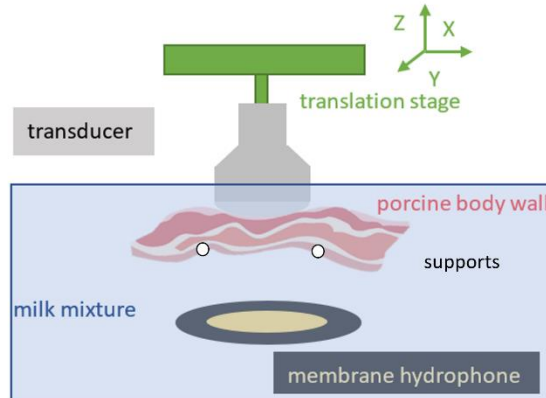


Figure 5.1: Experimental setup used to measure *in situ* PRP through a body wall sample. The transducer was fixed to a 3-axis translation stage. Pork body walls were secured against the transducer with two physical supports. The membrane hydrophone measuring pressure was submerged in a milk mixture that had attenuation matching that of human liver.

For *in situ* experiments, we used the experimental setup shown in Figure 5.1 to measure *in situ* PRP through porcine abdominal body wall samples. Fresh pork belly sections from the local grocery store were secured to the face of the curvilinear transducer with two supports from below. An attenuating evaporated milk solution modeling liver attenuation was used to allow for scanning hydrophone measurements below the body wall samples. The evaporated milk was tuned by dilution with water to an attenuation matching liver ($\alpha = 0.5$ dB/cm/MHz [77-79]). The experimental system was a Siemens Sequoia and a 5C1 curvilinear transducer (Siemens Ultrasound, Issaquah,

WA), with the transducer's transmit configuration being a single beam pulse inversion harmonic sequence focused down the center as described in Table 5.1. Since we did not expect the spatial coherence trends to change as a function of MI once electronic noise was negligible, we used a high MI to isolate the effects of aberration from experimental electronic noise. We used the maximum possible source pressures for this imaging configuration given software limits. This resulted in an MI of 2.25. We mounted the Siemens 5C1 curvilinear transducer to a computer-controlled Newport 3-axis translation stage (MM3000, Newport Corporation, Irvine, CA) to measure pressure throughout a $6 \times 9 \times 20$ mm ROI around the focus with $0.2 \times 0.5 \times 1$ mm spacing (lateral \times elevation \times axial). The output voltage waveform from the membrane hydrophone (Model 804, Acertara Acoustic Laboratories, Longmont, CO) was converted to pressures using magnitude deconvolution [83, 84] where frequency-dependent magnitude sensitivity of the hydrophone was accounted for using 1-20 MHz calibration.

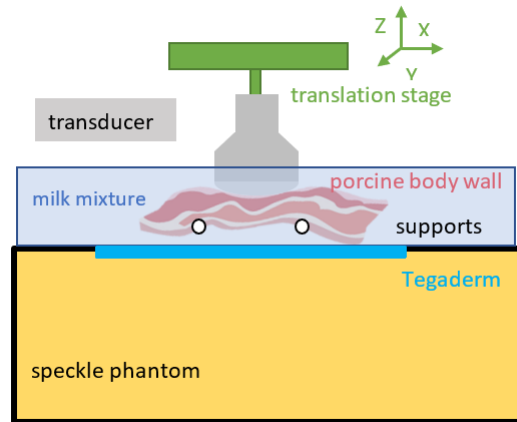


Figure 5.2: Experimental setup used to acquire channel data for spatial coherence values through a body wall sample. The pork belly and transducer were held in the same position relative to each other as in the PRP measurement setup shown in Figure 5.1. Data acquisition was performed with a customized toolset on the Sequoia scanner from a speckle generating phantom through a Tegaderm window at the base of the milk mixture container.

After measuring the *in situ* PRP, we measured the matching spatial coherence for each body wall sample using the setup shown in Figure 5.2. The transducer and pork belly were raised out of the hydrophone tank and placed in a tray filled with an evaporated milk and saline solution tuned to a sound speed of 1540 m/s as coupling medium. The bottom of the tray had a Tegaderm membrane (Model 1626W, 3M, Saint Paul, MN) 10 cm by 12 cm in size as an acoustic window to allow imaging of a speckle generating phantom with a 1540 m/s speed of sound (CIRS, Norfolk, VA). A thin layer of water (less than 1 mm) coupled the Tegaderm membrane to the phantom. The Siemens Sequoia scanner and 5C1 transducer used the same transmit configuration described in Table 5.1 as when measuring *in situ* PRP. Each body wall sample was translated 1.5 beamwidths (about 1.5 mm) laterally 10 times using the translation stage to acquire 10

independent speckle realizations for each transmit beam through the same body wall.

Pulse inverted channel data were collected to compute spatial coherence using Equation

5.4. Spatial coherence was then correlated with the measured *in situ* PRP.

5.2.3 Estimating Attenuation

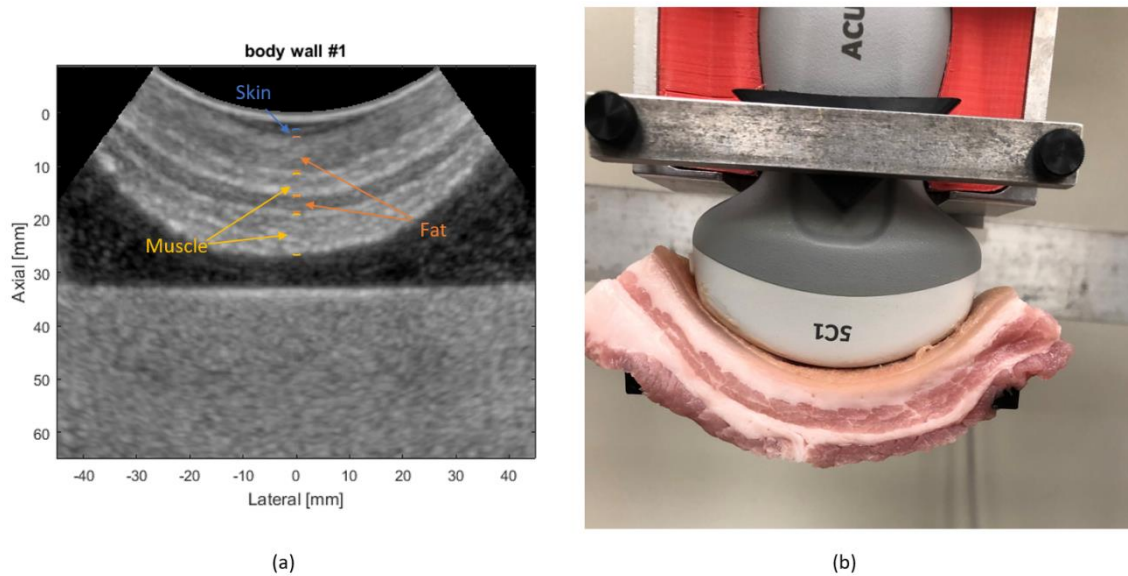


Figure 5.3: Example clinical b-mode image of a pork belly sample used to segment the various tissue thicknesses and to estimate the sample attenuation in (a). Layers shown are as follows: 1.5 mm skin, 6.9 mm fat, 4.6 mm muscle, 3.3 mm fat, and 8.2 mm muscle; The average attenuation estimate for the center line in the image was 0.61 dB/cm/MHz. (b) Photo of the corresponding pork belly sample mounted on to the transducer face.

Using both the B-mode and color photos taken during the experiment as shown in Figure 5.3, we manually segmented the layers of each pork body wall along the center b-mode line into 4 types of tissue: skin, fat, muscle, and liver. From the segmentations, we determined total thickness of skin, fat, muscle, and liver. We then applied attenuation coefficients found in literature (0.5, 0.4, 1.15, and 0.5 dB/cm/MHz for skin,

fat, muscle and liver, respectively [77-79]) to determine the estimated total attenuation through each body wall.

5.2.3 Multiple Linear Regression

Multiple linear regression was performed to assess the interaction of PRP/MIE with the following experimental variables: body wall attenuation, body wall thickness, body wall fat fraction, experimentally measured SLSC, and HSC.

5.3 Results

5.3.1 Simulation Results

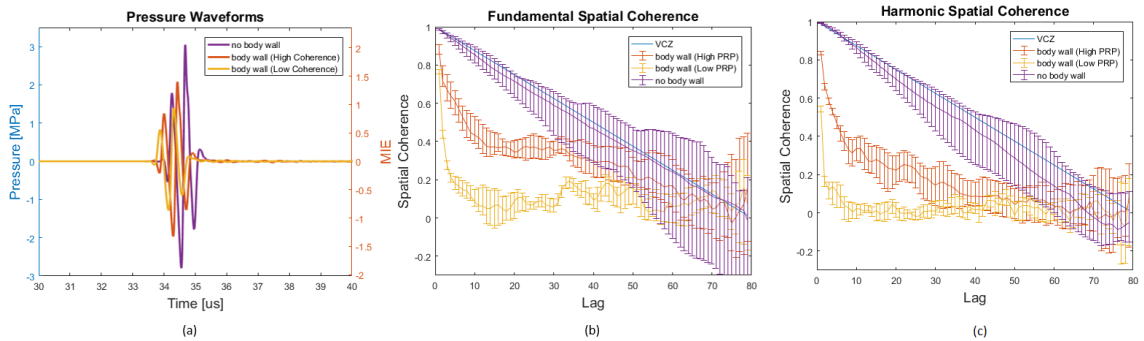


Figure 5.4: Matching simulated *in situ* PRP/MIE waveforms, fundamental spatial coherence, and harmonic spatial coherence. (a) Pressure traces from the location of maximum pulse intensity integral. MIEs were: 0.87(yellow trace), 1.3 (orange trace) and 1.9 (purple trace). (b) Example spatial coherence curves at the axial focus of 5cm for the received signal at the fundamental frequency. (c) Example spatial coherence curves at the axial focus of 5cm for the received signal at the harmonic frequency when pulse inversion is simulated. The blue line shows the ideal case with pure speckle predicted by the VCZ theorem. The purple line is the spatial coherence computed from a simulation through speckle and no body wall. The red line is from an example body wall that was associated with a relatively high PRP (MIE = 1.3). The yellow curve is from an example body wall that was associated with a relatively low PRP (MIE = 0.87). All error bars represent the median and interquartile range for 20 adjacent simulated lines.

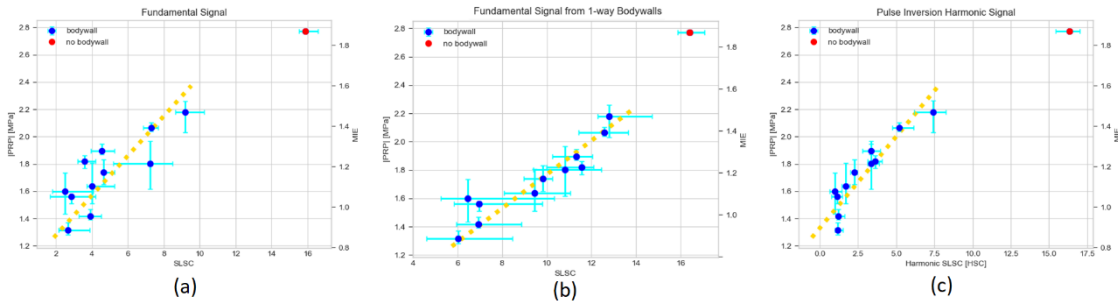


Figure 5.5: *In situ* PRP/MIE plotted against various spatial coherence metrics. (a) The *in situ* PRP/MIE plotted against the fundamental SLSC values (2-way body wall simulations). (b) The *in situ* PRP/MIE plotted against the SLSC values from the 1-way body wall simulations. (c) The simulated *in situ* PRP/MIE plotted against the Harmonic SLSC values. The points are the median values, while the error bars represent the interquartile range across 20 simulated adjacent lines through the same body wall. The red point is the ideal case without a body wall. The blue points are various body walls. The dotted yellow line represents the linear regression line of best fit computed using the median values from the body wall samples ($r^2 = 0.67$, $r^2 = 0.90$, and $r^2 = 0.85$).

5.3.1.1 Fundamental Spatial Coherence

The body walls decreased *in situ* PRP/ MIE as compared to the no body wall control case. Figure 5.4a illustrates pressure traces with MIEs decreasing from 1.9 for the control to 1.3 and 0.87 for two example body walls. Since attenuation differences between the 3 samples are within 5%, attenuation is not likely the source of decreased MIE magnitude. The fundamental spatial coherence curve for the no body wall control (purple) reasonably approximates that predicted by the VCZ theorem [60] (blue). Concurrently, the presence of body wall decreases the spatial coherence compared to the no body wall control (orange and yellow, Figure 5.4b). The body wall associated with the lower *in situ* PRP/MIE also has lower spatial coherence than the body wall associated with the higher *in situ* PRP/MIE.

Figure 5.5a demonstrates a strong linear correlation between fundamental SLSC and *in situ* PRP/MIE for the 11 simulated body wall samples ($r^2 = 0.67$). The no body wall control has the highest MIE (1.9) and the highest fundamental spatial coherence (median 15.8). The presence of body wall results in lower MIEs (between 0.87 and 1.45) and lower SLSCs (between 2.4 and 9.3).

5.3.1.2 1-way Body Wall Simulations

In situ PRP/MIE is a function of the forward propagating transmitted wave while the spatial coherence data is derived from the backscattered signal. Because the spatial coherence data is twice affected by the body walls compared to the *in situ* PRP/MIE, it is not expected to have perfect correlation with *in situ* PRP/MIE. We removed the effects of the body wall during the return trip to the transducer face by simulating 1-way body walls. The resulting relationship between SLSC from the 1-way body walls and *in situ* PRP/MIE are visualized in Figure 5.5b. Compared to the simulations of 2-way body walls shown in Figure 5.5a, *in situ* PRP/MIE remains unchanged, while the SLSC values for the simulated 1-way body walls are consistently higher than their 2-way counterparts, ranging between median values of 6 and 12.8, with the no body wall control median SLSC value being 16.2. The 1-way body wall SLSC values and corresponding *in situ* PRP/MIEs are highly correlated ($r^2 = 0.90$).

5.3.1.3 Harmonic Spatial Coherence

Experimentally and in clinical settings, 1-way body wall coherence measurements are not possible with a single pulse-echo transducer. As such, we explored with harmonic spatial coherence because the tissue harmonic signal is generated during propagation preferentially near the focus and bypasses some of the phase aberration during forward propagation to the focus. As such, we hypothesized that harmonic coherence may be more highly correlated with *in situ* PRP than fundamental coherence. Figure 5.4c shows harmonic spatial coherence data for the matched positions, body walls, and speckle realizations as in Figure 4b. Similar to the results from fundamental spatial coherence, the harmonic no body wall case (purple) retained the highest spatial coherence. Importantly, the body wall associated with a high *in situ* PRP/MIE (orange) exhibits higher spatial coherence than the body wall associated with a low *in situ* PRP/MIE (yellow). Harmonic spatial coherence values for the two body wall cases in Figure 5.4c are lower in magnitude than their fundamental counterparts in Figure 5.4b (1.4 vs. 2.8 and 7.2 vs. 9.3, respectively).

The correlation between Harmonic short lag Spatial Coherence (HSC) [81] and *in situ* PRP/MIE is examined in Figure 5.5c. HSC is computed by adding the first 20 lags shown in Figure 5.4c and plotted against *in situ* PRP/MIE for the 11 different body walls and the no body wall control. *In situ* PRP/MIE remains unchanged from Figure 5.5a. HSC for the no body wall control is 16.3, similar to both fundamental SLSC cases. HSC

values are consistently decreased for the body walls ranging between 1.2 and 7.5. The correlation between HSC and *in situ* PRP/MIE is strong ($r^2 = 0.85$). Table 5.3 shows that the regression coefficient calculated from HSC is higher than SLSC and just lower than SLSC with 1-way body walls.

5.3.2 Experimental Results

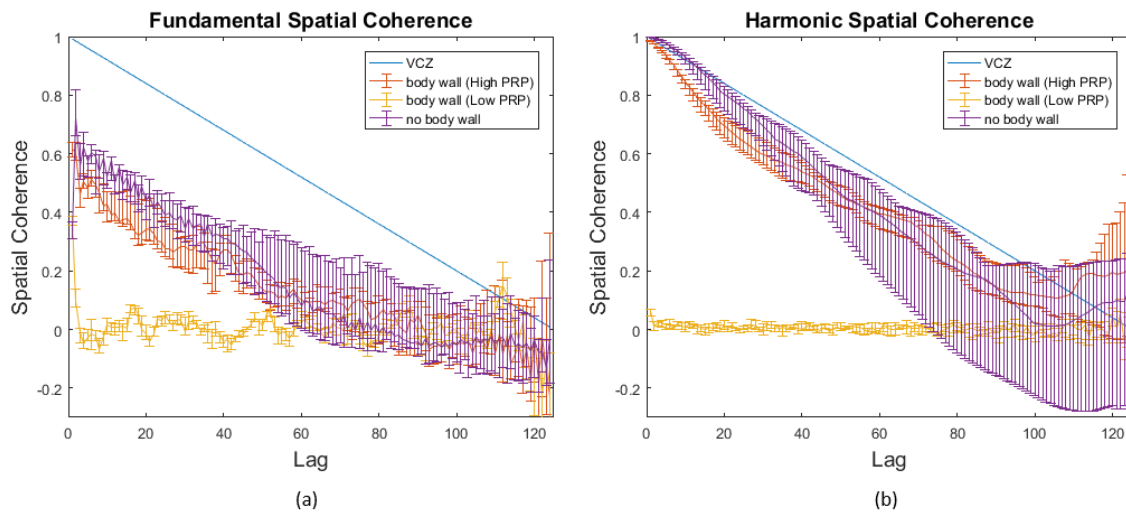


Figure 5.6: Example experimentally measured spatial coherence curves at the axial focus of 6cm in the speckle phantom for the received channel data at the fundamental (a) and harmonic (b) frequency when pulse inversion is employed. The blue line shows the ideal speckle case predicted by the VCZ theorem. The purple points are the spatial coherence computed when the propagation path only has milk and a Tegaderm membrane on top of the speckle phantom. The red points are from an example pork belly that was associated with a relatively high PRP (MIE = 1.49). The yellow points are from an example pork belly that was associated with a relatively low PRP (MIE = 0.51). All error bars represent the median and interquartile range for the same transmit line when the speckle phantom is translated across 10 independent speckle locations.

Figure 5.6a, b plot three example experimentally measured fundamental and harmonic spatial coherence curves at the 6 cm axial focus when assuming 1540 m/s

sound speed. Consistent with the simulation results, the no body wall control has the highest fundamental and harmonic spatial coherence amplitude (purple curves) and is the closest to the theoretical VCZ curve (blue curve). The body wall through which an *in situ* PRP magnitude of 1.88 MPa was measured has a fundamental and harmonic spatial coherence curve below the no body wall control (orange curves) and above the body wall with a lower corresponding *in situ* PRP magnitude of 0.65 MPa (yellow curves). The harmonic spatial coherence of the body wall with low PRP amplitude nears zeros, signifying minimal beamformer gain at the transmit focus for the measurement through this acoustic window.

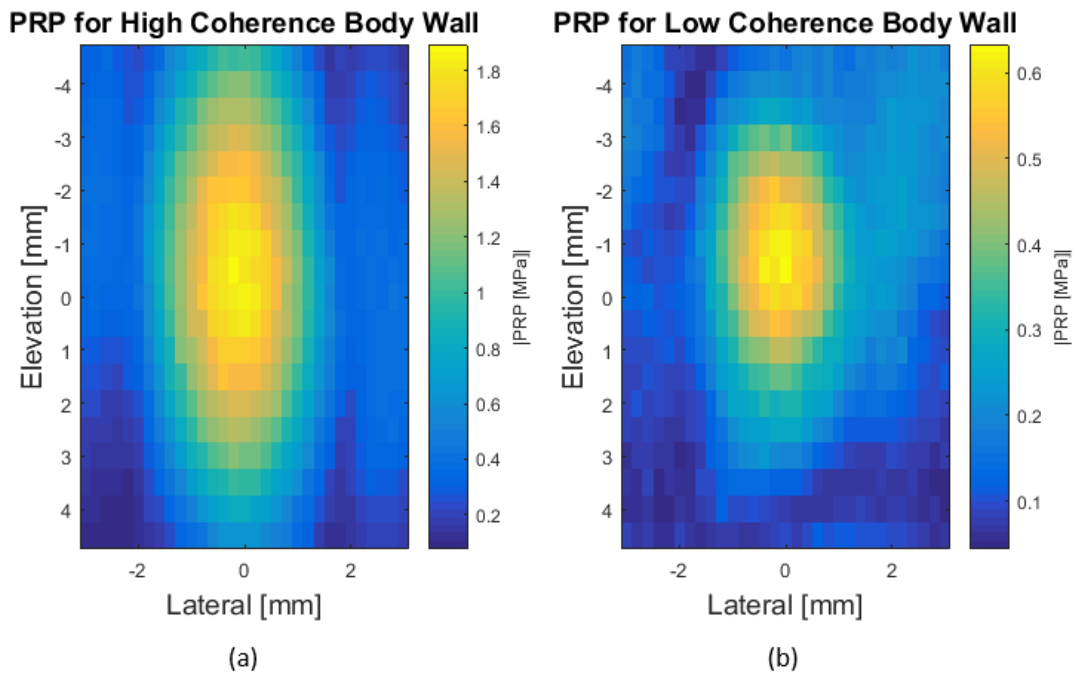


Figure 5.7: Coronal plane (elevation x lateral) map of the experimentally measured PRP magnitude at the axial depth of maximum PRP through (a) the high coherence body wall in Figure 5.6. (b) plots the same metric as (a), but for the low

coherence body wall in Figure 5.6. Note that these figures have different color bars, with much lower PRPs in (b), suggesting considerable defocusing for the low coherence body wall case.

Figure 5.7a, b map the lateral/elevation *in situ* PRP profiles (from the axial depth corresponding to the maximum PRP) for both the high and low spatial coherence body walls from Figure 5.6. Note that different color bar scales are used: the body wall with high spatial coherence has a higher PRP than that of the body wall with low spatial coherence.

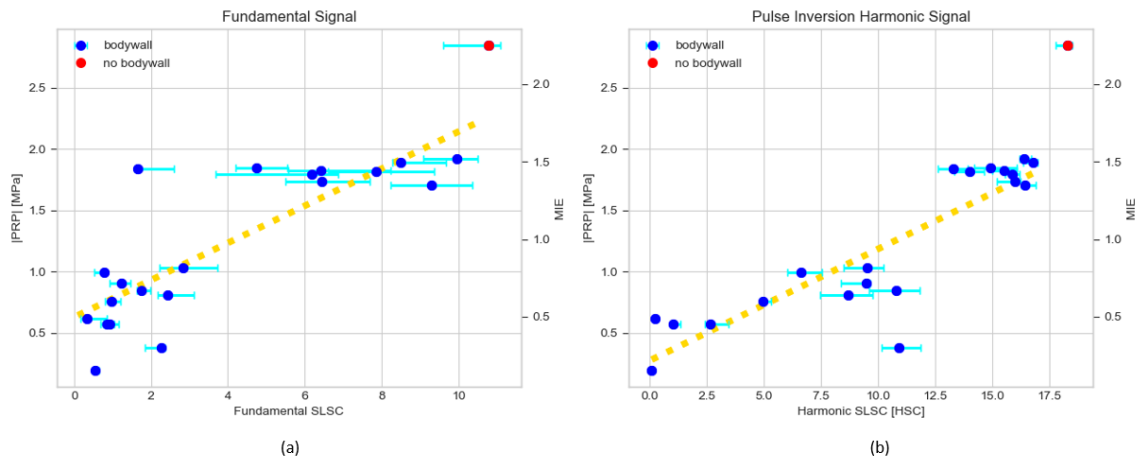


Figure 5.8: The experimentally measured *in situ* PRP/MIE plotted against the SLSC (a) and HSC (b) values computed by summing across the first 20 lags. The points are the median values, while the error bars represent the interquartile range across 10 speckle realizations from the same transmit line on the same pork belly section translated to different locations in the phantom. The red is the ideal case without a pork belly. The blue are various pork bellies. The dotted yellow line represents the linear regression line of best fit computed using the median values from all the pork belly samples. The r^2 of the fit is 0.67 for SLSC and 0.77 for HSC.

Figure 5.8a, b portray *in situ* PRP/MIE against SLSC and HSC measured experimentally for the 20 *ex vivo* body walls and the no body wall control, summing across the first 20 lags for both SLSC and HSC. The no body wall control has an MIE of

2.25 along with median SLSC and HSC of 10.8 and 18.2. The *ex vivo* body walls result in lower MIEs ranging between 0.23 and 1.52. SLSC was lowered to a range between 0.33 and 10.0 while HSC values were lowered to a range between 0.06 and 16.8 by the presence of the body walls. Linear regression of SLSC yielded a regression coefficient $r^2 = 0.67$ while regression of HSC yielded $r^2 = 0.77$.

Table 5.3: Regression Coefficient Between PRP/MIE and the Various Simulated Received Signals.

Signal	r^2
SLSC	0.67
HSC	0.85
SLSC w/ 1-way body wall	0.90

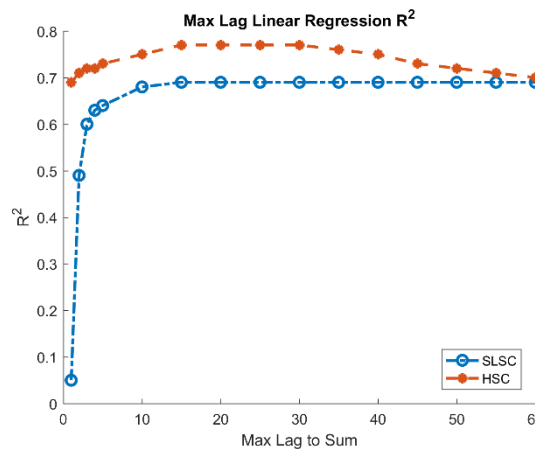


Figure 5.9: The r^2 value resulting from the linear regression line of best fit between experimentally measured spatial coherence and *in situ* PRP/MIE plotted vs. the maximum summation lag number used to compute SLSC and HSC. Red is the harmonic spatial coherence sum regression fit coefficient, while blue is the fundamental spatial coherence sum regression fit coefficient.

Investigators typically employ different summation maximum lags when computing the SLSC and HSC for imaging different organs for creating diagnostic images [81, 108]. As such, in developing our protocol we varied the summation maximum lag to determine the best range for correlation with *in situ* PRP/MIE. Figure 5.9 plots the r^2 from linear regressions between PRP and spatial coherence metrics when the maximum summation lag for HSC and SLSC was varied between 1 and 60. Both SLSC and HSC consistently have strong correlation with *in situ* PRP across a wide range of summed lags. For the HSC case, the regression coefficient peaks between 15 and 30 lags with $r^2 = 0.77$. For the SLSC case, the regression coefficient plateaus after summing the first 15 lags at $r^2 = 0.67$. Similar to the simulation results, HSC has higher correlation than SLSC with *in situ* PRP/MIE.

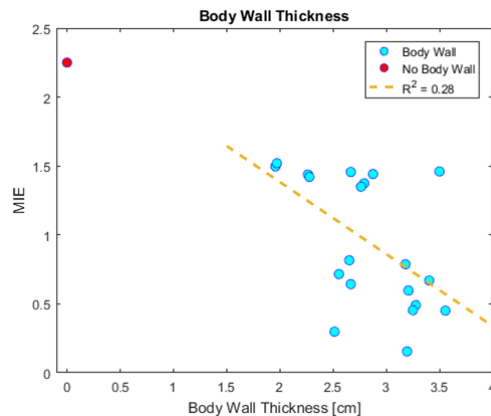


Figure 5.10: Pork belly thickness plotted with the corresponding MIE. Red is the case without a body wall present. Blue are the various pork body wall samples. The dotted yellow line is the linear regression line of best fit for all the pork belly samples. The regression coefficient is $r^2 = 0.28$.

Previous studies have suggested that body wall thickness may relate to the degradation of image quality [27, 107]. We investigated the correlation between MIE and body wall thickness for the 20 body walls in our experiment (Figure 5.10). Moderate correlation is found between MIE and body wall thickness ($r^2 = 0.28$).

Table 5.4: Multiple Linear Least Squares Model Fit. * Only HSC has a statistically significant impact on *in situ* PRP/MIE.

Term	Estimate	Standard error	t ratio	Prob. > t
HSC	0.069	0.023	2.99	0.0098 *
SLSC	0.066	0.042	1.59	0.1347
Body wall thickness (cm)	0.283	0.631	0.45	0.6614
Body wall fat fraction	-1.029	3.583	-0.29	0.7782
Total attenuation	4.806	20.431	0.24	0.8174

Table 5.4 shows the results of the multiple linear regression that we designed to assess the interaction of PRP/MIE with the experimental variables including: body wall thickness, body wall fat fraction, total body wall attenuation, SLSC, and HSC. Only HSC has a significant effect on *in situ* PRP ($p < 0.01$).

5.4 Discussion

Collectively, the results from our experiments and simulations identify a strong positive correlation between spatial coherence and *in situ* PRP/MIE. SLSC yields a linear regression r^2 value of 0.67 for both the simulation (Figure 5.5a) and experimental data (Figure 5.8a), while HSC yields higher regression r^2 values of 0.85 and 0.77 for the simulation (Figure 5.5c) and experimental data (Figure 5.8b), respectively.

Harmonic spatial coherence correlates better with *in situ* PRP/MIE in both simulations and *ex vivo* experiments than its fundamental counterpart (SLSC). Unlike *in situ* PRP/MIE which is solely the product of forward propagation, fundamental spatial coherence is derived from the backscattered echo which is the compounded result of both forward and back propagation. The backscattered echo is phase aberrated twice and confounded by high amplitude reverberation in the nearfield [21]. The 1-way body wall simulations, where the body walls were removed before simulating propagation from the focal depth back to the transducer, eliminated the second phase aberration by the body wall. Unsurprisingly, the linear correlation between SLSC and *in situ* PRP/MIE improved from $r^2 = 0.67$ to 0.9 under this simulated one-way body wall scenario, as seen in Figure 5.5b and Table 5.3. Although the harmonic spatial coherence data is also derived from the backscattered echo, it is a closer approximation of the 1-way body wall fundamental signal because the tissue harmonic signal is preferentially generated near the focus, largely bypassing the body wall during forward propagation and thus is largely unaffected by phase aberration and reverberation during forward propagation. The tissue harmonic signal is then fully phase aberrated during the return propagation through the body wall. Thus, we posit that the tissue harmonic signal used to compute harmonic spatial coherence more closely models the 1-way propagation affects that are relevant to *in situ* PRP/MIE. The simulated linear regression results are consistent with this hypothesis as they increase from $r^2 = 0.67$ for SLSC to 0.85 for HSC (Figure 5.5c),

similar to the simulated r^2 of 0.9 obtained for SLSC with 1-way body walls as seen in Figure 5.5b and Table 5.3.

In the simulated data, the range of SLSC, SLSC with 1-way body wall, and HSC values differ even though the values for the no body wall control remained around 16. The SLSC values for the 11 body walls in Figure 5.5a ranged between 2.4 and 9.3. The SLSC values increased for the matching 1-way body walls in Figure 5.5b ranging between 6 and 12.8. One reason for this increase can be attributed to the suppression of reverberation clutter which decreases coherence at all lags [61, 108]. Additionally, the lack of the second phase aberration by the body wall during return propagation also increased the coherence values. Unlike the SLSC with 1-way body walls, the simulated HSC decreased from the original SLSC values to a range between 1.2 and 7.5 even though it also suppressed reverberation clutter and was predominately phase aberrated on back propagation. This can be explained by differences in frequency. When the harmonic signal experiences the same speed of sound changes as the fundamental signal, the phase shift is twice that of the fundamental. As such, phase aberration was more pronounced in the harmonic coherence shown in the body walls of Figure 5.4c compared to the corresponding fundamental coherence curves in Figure 5.4b. In Figure 5.4b, c, the harmonic coherence values for the two body wall samples fall below 0.2 at lags 2 and 27 while the fundamental coherence drops below 0.2 at lags 5 and 50 respectively.

The experimentally measured fundamental spatial coherence values shown in Figure 5.6a have a sharp decrease at lag 1 for the no body wall case, much lower than that predicted by the VCZ theorem and the simulations (Figure 5.4b). The source of this artifact was determined to be the Tegaderm and phantom top membrane interface because of the planar multiple reflection artifacts visible in the channel data. The artifact was eliminated when we imaged into the phantom without the Tegaderm present. Furthermore, the artifact amplitude was consistent between body wall samples meaning the SLSC comparisons between body wall samples was valid. Since the artifact did not impact the harmonic signal (i.e., no planar multiple reflection in the channel data, and no sharp decline at lag 1 for the no body wall case in Figure 5.6b), we continued to use the Tegaderm membrane in our experimental protocol in order to hold the milk coupling solution that was tuned for attenuation and speed of sound.

As visualized in Figure 5.9, for both SLSC and HSC, the regression r^2 increases when increasing the number of lags included in the summation from 1 to 15. This regression improvement can be attributed to the increase of spatial frequencies sampled with increasing element spacing. The more dramatic regression improvement for SLSC compared to HSC can be attributed to the high reverberation clutter present in the lower lags of SLSC [21, 61].

HSC values from the *ex vivo* experimental data are lower than those from the simulation results. As seen in Figures 5.8 and 5.5, the regression coefficient r^2 decreases

from 0.85 of the simulation data to 0.77 for the experimental data. One source of decorrelation can be attributed to the 3D nature of the *ex vivo* data. Unlike the *ex vivo* data, the 2D simulations do not model the elevation dimension. The *ex vivo* body walls do extend in the elevation dimension; therefore, ideally, spatial coherence should be determined in both the lateral and the elevation dimensions. Figure 5.7a, b highlight differences in the experimentally measured lateral/elevation plane at the depth of the maximum PRP for 2 different body walls. Although Figure 5.7a has lower lateral side lobes, Figure 5.7b has a tighter elevational focus. Unfortunately, the 1D abdominal curvilinear array transducers currently available do not allow for elevation coherence to be measured experimentally.

Body wall thickness shows moderate negative correlation of $r^2 = 0.28$ with *in situ* PRP/MIE in Figure 5.10. This is consistent with our previous findings where Tissue Harmonic Image (THI) quality and harmonic shear wave yield have demonstrated moderate negative correlation with increasing liver capsule depth [27, 107]. One might extrapolate these findings, therefore, to hypothesize that *in situ* PRP/MIE will positively correlate with harmonic shear wave yield and b-mode image quality, although this still remains to be demonstrated. We expected the total attenuation in the body wall to affect *in situ* PRP/MIE because with or without a body wall, more highly attenuating media will lead to decreases *in situ* PRP/MIE for a given transmit configuration. However, our multiple linear least squares model (Table 5.4) did not find total attenuation to

significantly interact with *in situ* PRP/MIE. The range of total attenuation within the sample group of 20 body walls employed herein varied less than 20%.

Combining results from previous studies where elevated MI imaging resulted in harmonic images with moderate increases in diagnostic value [107], and in SWE measurements with considerable increases in measurement yield [27, 41], and where ultrasonic propagation through body walls corresponded to decreased *in situ* PRP/MIE compared to that predicted by MI, the findings herein suggest the potential to increase the transmit pressure to generate better diagnostic information while keeping the *in situ* PRP/MIE below that predicted by MI.

With the ability to compute spatial coherence in real-time using GPU acceleration demonstrated by *Hyun et. Al* [110], future work could leverage the correlation between HSC and MIE shown in Figure 5.9 and *in vivo* attenuation estimation techniques to develop algorithms to estimate MIE on a patient specific basis during real-time *in vivo* imaging to determine safe ranges of acoustic pressure increases.

5.5 Conclusions

This study investigated the relationship between spatial coherence and *in situ* PRP/MIE for tightly focused transmit configurations (F/1.5) using an abdominal curvilinear transducer. The spatial coherence derived metrics SLSC and HSC displayed strong positive linear correlation with *in situ* PRP/MIE. We found that HSC consistently correlated with *in situ* PRP/MIE with a higher linear correlation coefficient than SLSC

because the tissue harmonic signal bypassed the majority of the reverberation and phase aberration during forward propagation. This study identifies HSC as a potential parameter to include when estimating safe transmit pressure increases for *in vivo* abdominal imaging.

5.6 Acknowledgements

This work was supported by NIH Grant R01 EB022106. The authors would like to thank Anna Knight and Jinjin Wu for their help with JMP statistics software, as well as Siemens Healthcare USA, Ultrasound Division for their in-kind technical support.

6 Conclusions and Future Work

Harmonic imaging is often the default ultrasonic abdominal imaging configuration used for clinical diagnostic purposes because of its ability to generate images with less clutter than fundamental frequency images. A major pitfall for using the tissue harmonic signal, however, is the reduced electronic SNR which leads to shallower penetration depths compared to fundamental signal. The obvious solution to the electronic signal-to-noise ratio (SNR) issue is to increase transmit pressure which would in turn increase the Mechanical Index (MI). Previously, preliminary clinical studies comparing current MI level pulses with elevated MI pulses have found moderate improvements in B-mode image quality and substantial improvements in SWS yield in liver SWEI measurements when using high MI transmits.

This dissertation first focused on SWEI measurements. Chapter 3 extended the previous clinical study in a more controlled *in vitro* experimental setup using modern hardware and commercially available MTL-SWEI sequences. The effects of MI and body walls were individually examined with respect to the push and track beams independently. It was found that increasing MI for push beams improved SWS yield and decreased SWS estimation uncertainty. The same trends were seen with increasing track beam MIs. Additionally, it was discovered that the presence of body walls degrades MTL-SWEI tracking more severely than ARFI push pulses in terms of the resulting shear wave speed measurement success.

Chapter 4 quantified the impact of abdominal body wall on *in situ* peak rarefactional pressure (PRP) during diagnostic ultrasound imaging. Specifically, a short 2 cycle pulse representative of that used for shear wave tracking or B-mode imaging was examined. It was found that the presence of body wall could cause *in situ* PRP to be both underestimated and overestimated by the FDA recommended MI formulation depending on focal configuration. For a large aperture (F/1.5), linear derating was found to overestimate *in situ* PRP due to not accounting for phase aberration caused by body wall heterogeneity. For a medium sized aperture (F/3), linear derating was found to accurately estimate *in situ* PRP. For a small aperture (F/5), linear derating was found to underestimate *in situ* PRP due to a combination of effects from phase aberration and reverberation clutter. Since small apertures on clinical transducers are not capable of generating elevated MI, this underestimation of *in situ* PRP is not cause for concern. For larger apertures, where clinical transducers are capable of generating elevated MIs, it is possible to employ elevated MI transmits to improve image quality while remaining within the spirit of the FDA guidelines for *in situ* PRP.

In order to use elevated MI transmits through body walls, ideally the ultrasound imaging system must be able to adaptively change transmit pressures based on feedback from each body wall. To provide feedback, a metric must be developed to more accurately estimate *in situ* PRP. Since differences in PRP are mainly caused by phase

aberration and reverberation, spatial coherence, a metric that is sensitive to both effects and is also able to be quantified in real-time is an excellent candidate.

Chapter 5 investigated the relationship between spatial coherence and *in situ* PRP for tightly focused transmit configurations (F/1.5). Both fundamental and harmonic spatial coherence derived metrics were examined in the form of short-lag spatial coherence (SLSC) and harmonic short-lag spatial coherence (HSC). Both SLSC and HSC were found in simulations and experimental measurements to have strong positive correlation with *in situ* PRP. HSC consistently correlated more closely with *in situ* PRP compared to SLSC.

The work presented in this thesis identified pulse types within liver diagnostic SWEI sequences which are most impacted by the presence of body wall. Then, it examined how heterogeneous body walls affect wave propagation in the body and impact *in situ* PRP magnitude. Lastly, it explored a real-time metric that strongly correlates with *in situ* PRP. Although this thesis makes headway in bringing personalized medicine to diagnostic abdominal ultrasound, future work is needed for clinical application.

The work presented in Chapter 3 showed increasing SWS yield as a function of MI for both the push and track beams. The yields, however, did not yet reach a plateau as function of either push or track MI used when pushing and tracking through body walls. As such, additional sequences can be developed to encompass a higher upper

limit MI in order to capture the plateau SWS yield MIs. Additionally, the portion of the experiment which only used the DAX transducer can also be adapted for a clinical study in the future which would provide impactful human data during *in vivo* imaging. Furthermore, future work can utilize the current *in situ* experimental setup to compare STL, MTL, and plane wave tracking directly to give insight on the performance of each SWEI track beam type. Also possible is the *in situ* experimental ARF push comparison between using high MI short duration push and lower MI long duration push in order to optimize push efficiency.

The work presented in Chapter 4 examined the effects of heterogenous body wall on wave propagation and *in situ* PRP for a single frequency and at one pulse length. Extending the work in the future will encompass simulations and experimental validations with more transducer frequencies and apertures to see if the same trends extend to all clinically relevant transmit configurations. Additionally, similar future studies with comparisons between long and short pulses can provide insight on if ARF push excitations are affected to the same extent compared to short tracking and B-mode pulses.

Chapter 5 demonstrated how HSC, a metric that strongly correlates with *in situ* PRP, changes with respect to different body walls. Since HSC is computed from channel data, it can theoretically be computed for all diagnostic imaging transmits. With the ability to compute spatial coherence in real-time using GPU acceleration demonstrated

by Hyun et al. (2017), future work could leverage the correlation between HSC and *in situ* PRP and *in vivo* attenuation estimation techniques to develop algorithms to estimate *in situ* PRP on a patient specific basis during real-time *in vivo* imaging to determine safe ranges of acoustic pressure increases.

In summary, elevated MI imaging has the potential to provide improved diagnostic value for the increasingly popular clinical applications of SWE imaging. Doing so can be safely implemented on a patient and imaging window specific basis once a more accurate metric for estimating peak pressures is fully developed using the knowledge gained from this dissertation. The doors to the world personalized medicine in diagnostic ultrasound imaging are open!

References

- [1] Firestone FA. The Supersonic Reflectoscope, an Instrument for Inspecting the Interior of Solid Parts by Means of Sound Waves. *J Acoust Soc Am*. 1945;17:287–99.
- [2] Campbell S. A short history of sonography in obstetrics and gynaecology. *Facts Views Vis Obgyn*. 2013;5(3):213-229.
- [3] Wild JJ, Reid JM. Application of echo-ranging techniques to the determination of structure of biological tissues. *Science*. 1952 Feb 29;115(2983):226-30.
- [4] Wild JJ, Neal D. Use of high-frequency ultrasonic waves for detecting changes of texture in living tissues. *Lancet*. 1951 Mar 24;1(6656):655-7.
- [5] Woo J. A Short History of the Development of Ultrasound in Obstetrics and Gynecology, 2002.
- [6] Nightingale KR, Palmeri ML, Nightingale RW, Trahey GE. On the feasibility of remote palpation using acoustic radiation force. *J Acoust Soc Am*. 2001;110:625–34.
- [7] Sarvazyan AP, Rudenko OV, Swanson SD, Fowlkes JB, Emelianov SY. Shear wave elasticity imaging: a new ultrasonic technology of medical diagnostics. *Ultrasound Med Biol*. 1998 Nov;24(9):1419-35.
- [8] Christopher T. Experimental investigation of finite amplitude distortion-based, second harmonic pulse echo ultrasonic imaging. *IEEE Trans Ultrason Ferroelectr Freq Control*. 1998;45(1):158-62.
- [9] Desser TS, Jeffrey RB. Tissue harmonic imaging techniques: physical principles and clinical applications. *Semin Ultrasound CT MR*. 2001 Feb;22(1):1-10.
- [10] Caraianni C, Yi D, Petrescu B, Dietrich C. Indications for abdominal imaging: When and what to choose? *J Ultrason*. 2020;20(80):e43-e54.
- [11] Mishra P, Younossi ZM. Abdominal ultrasound for diagnosis of nonalcoholic fatty liver disease (NAFLD). *Am J Gastroenterol*. 2007 Dec;102(12):2716-7.
- [12] Asham EH, Kaseb A, Ghobrial RM. Management of hepatocellular carcinoma. *Surg Clin North Am*. 2013 Dec;93(6):1423-50.

- [13] Bruix J, Sherman M; American Association for the Study of Liver Diseases. Management of hepatocellular carcinoma: an update. *Hepatology*. 2011 Mar;53(3):1020-2.
- [14] Joshi K, Mendler M, Gish R, Loomba R, Kuo A, Patton H, Kono Y. Hepatocellular carcinoma surveillance: a national survey of current practices in the USA. *Dig Dis Sci*. 2014 Dec;59(12):3073-7.
- [15] Virmani J, Kumar V, Kalra N, Khandelwal N. Characterization of primary and secondary malignant liver lesions from B-mode ultrasound. *J Digit Imaging*. 2013 Dec;26(6):1058-70.
- [16] Singal AG, Nehra M, Adams-Huet B, Yopp AC, Tiro JA, Marrero JA, Lok AS, Lee WM. Detection of hepatocellular carcinoma at advanced stages among patients in the HALT-C trial: where did surveillance fail? *Am J Gastroenterol*. 2013 Mar;108(3):425-32.
- [17] Sporea I, Bota S, Săftoiu A, Şirli R, Gradinăru-Taşcău O, Popescu A, Lupşor Platon M, Fierbinteanu-Braticevici C, Gheonea DI, Săndulescu L, Badea R; Romanian Society of Ultrasound in Medicine and Biology. Romanian national guidelines and practical recommendations on liver elastography. *Med Ultrason*. 2014 Jun;16(2):123-38.
- [18] Klysik M, Garg S, Pokharel S, Meier J, Patel N, Garg K. Challenges of imaging for cancer in patients with diabetes and obesity. *Diabetes Technol Ther*. 2014 Apr;16(4):266-74.
- [19] Schuh S, Man C, Cheng A, Murphy A, Mohanta A, Moineddin R, Tomlinson G, Langer JC, Doria AS. Predictors of non-diagnostic ultrasound scanning in children with suspected appendicitis. *J Pediatr*. 2011 Jan;158(1):112-8.
- [20] Ogden CL, Carroll MD, Kit BK, Flegal KM. Prevalence of childhood and adult obesity in the United States, 2011-2012. *JAMA*. 2014 Feb 26;311(8):806-14.
- [21] Thomas JD, Rubin DN. Tissue harmonic imaging: why does it work? *J Am Soc Echocardiogr*. 1998 Aug;11(8):803-8.
- [22] Christopher T. Finite amplitude distortion-based inhomogeneous pulse echo ultrasonic imaging. *IEEE Trans Ultrason Ferroelectr Freq Control*. 1997;44(1):125-39.
- [23] Bradley C. Mechanisms of image quality improvement in tissue harmonic imaging. *AIP Conf Proc*. 2006; 838: 247-254

- [24] Pinton GF, Trahey GE, Dahl JJ. Sources of image degradation in fundamental and harmonic ultrasound imaging using nonlinear, full-wave simulations. *IEEE Trans Ultrason Ferroelectr Freq Control*. 2011 Apr;58(4):754-65.
- [25] Center for Devices and Radiological Health (CDRH). 510(k) Guide for Measuring and Reporting Acoustic Output of Diagnostic Ultrasound Medical Devices. US Dept of Health and Human Services 1985, Rev. 1993, December 1994.
- [26] AIUM/NEMA. Standard for Real-Time Display of Thermal and Mechanical Acoustic Output Indices on Diagnostic Ultrasound Equipment, 1992.
- [27] Deng Y, Palmeri ML, Rouze NC, Haystead CM, Nightingale KR. Evaluating the Benefit of Elevated Acoustic Output in Harmonic Motion Estimation in Ultrasonic Shear Wave Elasticity Imaging. *Ultrasound Med Biol*. 2018 Feb;44(2):303-310.
- [28] Deng Y, Palmeri ML, Rouze NC, Rosenzweig SJ, Abdelmalek MF, Nightingale KR. Analyzing the Impact of Increasing Mechanical Index and Energy Deposition on Shear Wave Speed Reconstruction in Human Liver. *Ultrasound Med Biol*. 2015 Jul;41(7):1948-57.
- [29] Elegbe EC, McAleavey SA. Single tracking location methods suppress speckle noise in shear wave velocity estimation. *Ultrason Imaging*. 2013 Apr;35(2):109-25.
- [30] Hollender P, Lipman SL, Trahey GE. Three-Dimensional Single-Track-Location Shear Wave Elasticity Imaging. *IEEE Trans Ultrason Ferroelectr Freq Control*. 2017 Dec;64(12):1784-1794.
- [31] Palmeri ML, Rouze NC, Wang MH, Ding X, Nightingale KR. Quantifying the impact of shear wavelength and kernel size on shear wave speed estimation. *Ultrasonics Symposium (IUS)*; 2010. pp. 13–16.
- [32] Rouze NC, Wang MH, Palmeri ML, Nightingale KR. Parameters affecting the resolution and accuracy of 2-D quantitative shear wave images. *IEEE Trans Ultrason Ferroelectr Freq Control*. 2012 Aug;59(8):1729-40.
- [33] American Institute of Ultrasound in Medicine/National Electrical Manufacturers Association (AIUM/NEMA). Acoustic output measurement standard for diagnostic ultrasound equipment. Laurel, MD/Rosslyn, VA; 1998.
- [34] Nightingale K. Acoustic Radiation Force Impulse (ARFI) Imaging: a Review. *Curr Med Imaging Rev*. 2011 Nov 1;7(4):328-339.

- [35] Shiina T, Nightingale KR, Palmeri ML, Hall TJ, Bamber JC, Barr RG, Castera L, Choi BI, Chou YH, Cosgrove D, Dietrich CF, Ding H, Amy D, Farrokh A, Ferraioli G, Filice C, Friedrich-Rust M, Nakashima K, Schafer F, Sporea I, Suzuki S, Wilson S, Kudo M. WFUMB guidelines and recommendations for clinical use of ultrasound elastography: Part 1: basic principles and terminology. *Ultrasound Med Biol.* 2015 May;41(5):1126-47.
- [36] Palmeri ML, Miller ZA, Glass TJ, Garcia-Reyes K, Gupta RT, Rosenzweig SJ, Kauffman C, Polascik TJ, Buck A, Kulbacki E, Madden J, Lipman SL, Rouze NC, Nightingale KR. B-mode and acoustic radiation force impulse (ARFI) imaging of prostate zonal anatomy: comparison with 3T T2-weighted MR imaging. *Ultrasound Imaging.* 2015 Jan;37(1):22-41.
- [37] Rosenzweig SJ, Palmeri ML, Rouze NC, Lipman SL, Kulbacki E, Madden J, Polascik TJ, Nightingale KR. Comparison of concurrently acquired in vivo 3D ARFI and SWEI images of the prostate. *IEEE Int. Ultrason. Symp. IUS, 2012*;97-100.
- [38] Morris DC, Chan DY, Lye TH, Chen H, Palmeri ML, Polascik TJ, Foo WC, Huang J, Mamou J, Nightingale KR. Multiparametric Ultrasound for Targeting Prostate Cancer: Combining ARFI, SWEI, QUS and B-Mode. *Ultrasound Med Biol.* 2020 Dec;46(12):3426-3439.
- [39] Rouze NC, Wang MH, Palmeri ML, Nightingale KR. Robust estimation of time-of-flight shear wave speed using a radon sum transformation. *IEEE Trans Ultrason Ferroelectr Freq Control.* 2010 Dec;57(12):2662-70.
- [40] Deng Y, Rouze NC, Palmeri ML, Nightingale KR. Ultrasonic Shear Wave Elasticity Imaging Sequencing and Data Processing Using a Verasonics Research Scanner. *IEEE Trans Ultrason Ferroelectr Freq Control.* 2017 Jan;64(1):164-176.
- [41] Wang MH, Palmeri ML, Rotemberg VM, Rouze NC, Nightingale KR. Improving the robustness of time-of-flight based shear wave speed reconstruction methods using RANSAC in human liver in vivo. *Ultrasound Med Biol.* 2010 May;36(5):802-13.
- [42] Jin FQ, Carlson FC, Hall TJ, Feltovich H, Palmeri ML. Deep learning based quantitative uncertainty estimation for ultrasound shear wave elasticity imaging. *IEEE Int. Ultrason. Symp. IUS, 2021.*

- [43] Nightingale K, McAleavey S, Trahey G. Shear-wave generation using acoustic radiation force: in vivo and ex vivo results. *Ultrasound Med Biol.* 2003 Dec;29(12):1715-23.
- [44] Lizzi FL, Greenebaum M, Feleppa EJ, Elbaum M, Coleman DJ. Theoretical framework for spectrum analysis in ultrasonic tissue characterization. *J Acoust Soc Am.* 1983 Apr;73(4):1366-73.
- [45] Nyborg WLM. Acoustic Streaming. *Physical Acoustics*, 1965;2:265–331.
- [46] Hollender P, Rosenzweig SJ, Nightingale KR, Trahey GE. Micro-elasticity (μ -E): CNR and resolution of acoustic radiation force impulse imaging and single- and multiple track location shear wave elasticity imaging for visualizing small targets. *IEEE Int. Ultrason. Symp. IUS*, 2014;703-706.
- [47] Gennisson JL, Provost J, Deffieux T, Papadacci C, Imbault M, Pernot M, Tanter M. 4-D ultrafast shear-wave imaging. *IEEE Trans Ultrason Ferroelectr Freq Control.* 2015 Jun;62(6):1059-65.
- [48] Doherty JR, Dahl JJ, Trahey GE. Harmonic tracking of acoustic radiation force-induced displacements. *IEEE Trans Ultrason Ferroelectr Freq Control.* 2013 Nov;60(11):2347-58.
- [49] Walker WF, Trahey GE. The application of k-space in pulse echo ultrasound. *IEEE Trans Ultrason Ferroelectr Freq Control.* 1998;45(3):541-58.
- [50] Amador C, Song P, Meixner DD, Chen S, Urban MW. Improvement of Shear Wave Motion Detection Using Harmonic Imaging in Healthy Human Liver. *Ultrasound Med Biol.* 2016 May;42(5):1031-41.
- [51] Walker WF, Trahey GE, A Fundamental Limit on Delay Estimation Using Partially Correlated Speckle Signals. *IEEE Trans Ultrason Ferroelectr Freq Control.* 1995 March;42(2): 301-8.
- [52] Carstensen EL. Acoustic cavitation and the safety of diagnostic ultrasound. *Ultrasound Med Biol.* 1987 Oct;13(10):597-606.
- [53] Holland CK, Apfel RE. Thresholds for transient cavitation produced by pulsed ultrasound in a controlled nuclei environment. *J Acoust Soc Am.* 1990 Nov;88(5):2059-69.
- [54] Nightingale KR, Church CC, Harris G, Wear KA, Bailey MR, Carson PL, Jiang H, Sandstrom KL, Szabo TL, Ziskin MC. Conditionally Increased Acoustic

Pressures in Nonfetal Diagnostic Ultrasound Examinations Without Contrast Agents: A Preliminary Assessment. *J Ultrasound Med.* 2015 Jul;34(7):1-41.

- [55] Irshad A, Anis M, Ackerman SJ. Current role of ultrasound in chronic liver disease: surveillance, diagnosis and management of hepatic neoplasms. *Curr Probl Diagn Radiol.* 2012 Mar-Apr;41(2):43-51.
- [56] Kono Y, Joshi K, Richman K, O'Boyle M. Ultrasound In HCC Surveillance: What Is The Quality Of Ultrasound And What Factors Affect Quality? Ultrasound in Medicine & Biology, *Ultrasound Med Biol.* 2015 April;41(4):S17.
- [57] Desser TS, Jedrzejewicz T, Bradley C. Native tissue harmonic imaging: basic principles and clinical applications. *Ultrasound Quarterly*, 16(1):40-48, 2000.
- [58] van Cittert PH. Die Wahrscheinliche Schwingungsverteilung in Einer von Einer Lichtquelle Direkt Oder Mittels Einer Linse Beleuchteten Ebene. *Physica.* 1934;1 (1-6): 201-210.
- [59] Zernike F. The concept of degree of coherence and its application to optical problems. *Physica.* 1938;5(8): 785-795.
- [60] Mallart R, Fink M. Adaptive focusing in scattering media through sound-speed inhomogeneities: The van cittert zernike approach and focusing criterion. *J Acoust Soc Am.* 1994;96(6):3721-32.
- [61] Pinton GF, Trahey GE, Dahl JJ. Spatial coherence in human tissue: Implications for imaging and measurement. *IEEE Trans Ultrason Ferroelectr Freq Control.* 2014; 61(12):1976-1987
- [62] Long W, Bottenus N, Trahey GE. Lag-One Coherence as a Metric for Ultrasonic Image Quality. *IEEE Trans Ultrason Ferroelectr Freq Control.* 2018 Oct;65(10):1768-1780.
- [63] Rockey DC, Caldwell SH, Goodman ZD, Nelson RC, Smith AD; American Association for the Study of Liver Diseases. Liver biopsy. *Hepatology.* 2009 Mar;49(3):1017-44.
- [64] Goodman ZD. Grading and staging systems for inflammation and fibrosis in chronic liver diseases. *J Hepatol.* 2007 Oct;47(4):598-607.
- [65] Manning DS, Afdhal NH. Diagnosis and quantitation of fibrosis. *Gastroenterology.* 2008 May;134(6):1670-81.

- [66] Piccinino F, Sagnelli E, Pasquale G, Giusti G. Complications following percutaneous liver biopsy. A multicentre retrospective study on 68,276 biopsies. *J Hepatol.* 1986;2(2):165-73.
- [67] Bedossa P, Dargère D, Paradis V. Sampling variability of liver fibrosis in chronic hepatitis C. *Hepatology.* 2003 Dec;38(6):1449-57.
- [68] Regev A, Berho M, Jeffers LJ, Milikowski C, Molina EG, Pylsopoulos NT, Feng ZZ, Reddy KR, Schiff ER. Sampling error and intraobserver variation in liver biopsy in patients with chronic HCV infection. *Am J Gastroenterol.* 2002 Oct;97(10):2614-8.
- [69] van Katwyk S, Coyle D, Cooper C, Pussegoda K, Cameron C, Skidmore B, Brenner S, Moher D, Thavorn K. Transient elastography for the diagnosis of liver fibrosis: a systematic review of economic evaluations. *Liver Int.* 2017 Jun;37(6):851-861.
- [70] Wang MH, Palmeri ML, Guy CD, Yang L, Hedlund LW, Diehl AM, Nightingale KR. In vivo quantification of liver stiffness in a rat model of hepatic fibrosis with acoustic radiation force. *Ultrasound Med Biol.* 2009 Oct;35(10):1709-21.
- [71] Schmeltzer PA, Talwalkar JA. Noninvasive tools to assess hepatic fibrosis: ready for prime time? *Gastroenterol Clin North Am.* 2011 Sep;40(3):507-21.
- [72] Castéra L, Vergniol J, Foucher J, Le Bail B, Chanteloup E, Haaser M, Darriet M, Couzigou P, De Ledinghen V. Prospective comparison of transient elastography, Fibrotest, APRI, and liver biopsy for the assessment of fibrosis in chronic hepatitis C. *Gastroenterology.* 2005 Feb;128(2):343-50.
- [73] Kim HJ, Lee HK, Cho JH, Yang HJ. Quantitative comparison of transient elastography (TE), shear wave elastography (SWE) and liver biopsy results of patients with chronic liver disease. *J Phys Ther Sci.* 2015 Aug;27(8):2465-8.
- [74] Ferraioli G, Filice C, Castera L, Choi BI, Sporea I, Wilson SR, Cosgrove D, Dietrich CF, Amy D, Bamber JC, Barr R, Chou YH, Ding H, Farrokh A, Friedrich-Rust M, Hall TJ, Nakashima K, Nightingale KR, Palmeri ML, Schafer F, Shiina T, Suzuki S, Kudo M. WFUMB guidelines and recommendations for clinical use of ultrasound elastography: Part 3: liver. *Ultrasound Med Biol.* 2015 May;41(5):1161-79.

- [75] Carrascal CA, Aristizabal S, Greenleaf JF, Urban MW. Phase Aberration and Attenuation Effects on Acoustic Radiation Force-Based Shear Wave Generation. *IEEE Trans Ultrason Ferroelectr Freq Control*. 2016 Feb;63(2):222-32.
- [76] Pinton G. Ultrasound imaging with three dimensional full-wave nonlinear acoustic simulations. Part 2: sources of image degradation in intercostal imaging, 2020.
- [77] Chivers RC, Hill CR. Ultrasonic attenuation in human tissue. *Ultrasound Med Biol*. 1975 Oct;2(1):25-9.
- [78] Duck FA. Physical Properties of Tissue: a Comprehensive Reference Book. *Institute of Physics and Engineering in Medicine*, 2012.
- [79] Bamber JC, Hill CR. Ultrasonic attenuation and propagation speed in mammalian tissues as a function of temperature. *Ultrasound Med Biol*. 1979;5(2):149-57.
- [80] Napolitano DJ, Cole CR, Holley JL, Hossack JA, Bradley CE, Phillips P. Diagnostic ultrasound imaging method and system with improved frame rate (U.S. Patent No. 10/081,978). U.S. Patent and Trademark Office. 2000.
- [81] Dahl J, Jakovljevic M, Pinton GF, Trahey GE. Harmonic spatial coherence imaging: an ultrasonic imaging method based on backscatter coherence. *IEEE Trans Ultrason Ferroelectr Freq Control*. 2012 Apr;59(4):648-59.
- [82] Kasai C, Koroku N, Koyano A, Omoto R. Real-Time Two-Dimensional Blood Flow Imaging Using an Autocorrelation Technique. *IEEE Trans Ultrason Ferroelectr Freq Control*. 1985 May;32(3):458-463.
- [83] Wear KA, Gammell PM, Maruvada S, Liu Y, Harris GR. Improved measurement of acoustic output using complex deconvolution of hydrophone sensitivity. *IEEE Trans Ultrason Ferroelectr Freq Control*. 2014 Jan;61(1):62-75.
- [84] International electrotechnical commision. IEC 62359: Ultrasonics Field characterization Test methods for the determination International Electrotechnical Commission, Geneva, Switzerland, 2nd edition, 2010.
- [85] Smith SW, Insana MF, Lopez H. New contrast-detail phantoms for improved precision in lesion detection measurements. *Ultrasound Med Biol*. 1989;15(4):383-93.

- [86] Treeby BE, Zhang EZ, Thomas AS, Cox BT. Measurement of the ultrasound attenuation and dispersion in whole human blood and its components from 0-70 MHz. *Ultrasound Med Biol.* 2011 Feb;37(2):289-300.
- [87] Hamilton MF, Blackstock DT. Nonlinear Acoustics. Tech. rep., 2008.
- [88] Pinton GF, Dahl J, Rosenzweig S, Trahey GE. A heterogeneous nonlinear attenuating full-wave model of ultrasound. *IEEE Trans Ultrason Ferroelectr Freq Control.* 2009 Mar;56(3):474-88.
- [89] Pinton GF. Ultrasound imaging of the human body with three dimensional full-wave nonlinear acoustics. Part 1: simulations methods, 2020.
- [90] Spitzer V, Ackerman MJ, Scherzinger AL, Whitlock D. The visible human male: a technical report. *J Am Med Inform Assoc.* 1996 Mar-Apr;3(2):118-30.
- [91] Wells PNT. Ultrasonic imaging of the human body. *Reports on Progress in Physics.* 1999;62:671-722.
- [92] Mast TD, Hinkelman LM, Orr MJ, Waag RC. The effect of abdominal wall morphology on ultrasonic pulse distortion. Part II. Simulations. *J Acoust Soc Am.* 1998 Dec;104(6):3651-64.
- [93] Szabo TL, Szabo TL. Chapter 1 – Introduction. *Diagnostic Ultrasound Imaging: Inside Out.* 2014;2012:1-37.
- [94] Szabo TL, Lewin PA. Ultrasound transducer selection in clinical imaging practice. *J Ultrasound Med.* 2013 Apr;32(4):573-82.
- [95] Jensen JA, Nikolov SI, Gammelmark KL, Pedersen MH. Synthetic aperture ultrasound imaging. *Ultrasonics.* 2006 Dec 22;44 Suppl 1:e5-15.
- [96] Preston RC, Bacon DR, Smith RA. Calibration of medical ultrasonic equipment-procedures and accuracy assessment. *IEEE Trans Ultrason Ferroelectr Freq Control.* 1988;35(2):110-21.
- [97] Ziskin MC. Specification of acoustic output level and measurement uncertainty in ultrasonic exposimetry. *IEEE Trans Ultrason Ferroelectr Freq Control.* 2003 Aug;50(8):1023-34.
- [98] ONDA. Hydrophone Calibrations Calibration. Tech. rep., 2013.

- [99] Walker WF, Trahey GE. Speckle coherence and implications for adaptive imaging. *J Acoust Soc Am*. 1997 Apr;101(4):1847-58.
- [100] Park H, Park JY, Kim DY, Ahn SH, Chon CY, Han KH, Kim SU. Characterization of focal liver masses using acoustic radiation force impulse elastography. *World J Gastroenterol*. 2013 Jan 14;19(2):219-26.
- [101] Yoon JH, Lee JM, Han JK, Choi BI. Shear wave elastography for liver stiffness measurement in clinical sonographic examinations: evaluation of intraobserver reproducibility, technical failure, and unreliable stiffness measurements. *J Ultrasound Med*. 2014 Mar;33(3):437-47.
- [102] Su TH, Liao CH, Liu CH, Huang KW, Tseng TC, Yang HC, Liu CJ, Chen PJ, Chen DS, Kao JH. Acoustic Radiation Force Impulse US Imaging: Liver Stiffness in Patients with Chronic Hepatitis B with and without Antiviral Therapy. *Radiology*. 2018 Jul;288(1):293-299.
- [103] Bruno C, Minniti S, Bucci A, Pozzi Mucelli R. ARFI: from basic principles to clinical applications in diffuse chronic disease-a review. *Insights Imaging*. 2016 Oct;7(5):735-46.
- [104] Yeom SK, Lee CH, Cha SH, Park CM. Prediction of liver cirrhosis, using diagnostic imaging tools. *World J Hepatol*. 2015 Aug 18;7(17):2069-79.
- [105] de Moura Almeida A, Cotrim HP, Barbosa DB, de Athayde LG, Santos AS, Bitencourt AG, de Freitas LA, Rios A, Alves E. Fatty liver disease in severe obese patients: diagnostic value of abdominal ultrasound. *World J Gastroenterol*. 2008 Mar 7;14(9):1415-8.
- [106] Schuh S, Man C, Cheng A, Murphy A, Mohanta A, Moineddin R, Tomlinson G, Langer JC, Doria AS. Predictors of non-diagnostic ultrasound scanning in children with suspected appendicitis. *J Pediatr*. 2011 Jan;158(1):112-8.
- [107] Deng Y, Palmeri ML, Rouze NC, Trahey GE, Haystead CM, Nightingale KR. Quantifying Image Quality Improvement Using Elevated Acoustic Output in B-Mode Harmonic Imaging. *Ultrasound Med Biol*. 2017 Oct;43(10):2416-2425.
- [108] Lediju MA, Trahey GE, Byram BC, Dahl JJ. Short-lag spatial coherence of backscattered echoes: imaging characteristics. *IEEE Trans Ultrason Ferroelectr Freq Control*. 2011 Jul;58(7):1377-88.

- [109] Miller DL, Dou C, Wiggins RC. Contrast-enhanced diagnostic ultrasound causes renal tissue damage in a porcine model. *J Ultrasound Med.* 2010 Oct;29(10):1391-401.
- [110] Hyun D, Crowley AL, Dahl JJ. Efficient Strategies for Estimating the Spatial Coherence of Backscatter. *IEEE Trans Ultrason Ferroelectr Freq Control.* 2017 Mar;64(3):500-513.

Biography

Bofeng Zhang graduated from high school in Northville, Michigan before attending Johns Hopkins University in 2011. He graduated from college in 2015 with a B.S. in Biomedical Engineering and a minor in Computer Science. In the fall of 2015, Bofeng began pursuing a Ph.D. in Biomedical Engineering at Duke University under the guidance of Dr. Kathryn R. Nightingale. During graduate school, Bofeng participated in an internship with the ultrasound division of the Siemens Healthineers in Issaquah, Washington in the fall/winter of 2017.

Selected Publications:

- **Zhang B**, Pinton GF, Deng Y, Nightingale KR. Quantifying the Effect of Abdominal Body Wall on In Situ Peak Rarefaction Pressure During Diagnostic Ultrasound Imaging. *Ultrasound Med Biol*. 2021 Jun;47(6):1548-1558. doi: 10.1016/j.ultrasmedbio.2021.01.028. Epub 2021 Mar 13.
- **Zhang B**, Pinton GF, Nightingale KR. On the Relationship between Spatial Coherence and In Situ Pressure for Abdominal Imaging. *Ultrasound Med Biol*. 2021 Aug;47(8):2310-2320. doi: 10.1016/j.ultrasmedbio.2021.03.008. Epub 2021 May 11.